ACKNOWLEDGMENTS

I would like to thank my adviser, Dr. Charles W. Myles for his patience and advice during my time at Texas Tech University. I also wish to thank Dr. Harold P. Hjalmarson for his tireless interest in this project, and his willingness to share his advice and experience in both Physics and in life in general.

I would also like at this point to thank Dr. Samsoo Kang. Not only was he a valued collaborator when I started this research, his work in this area laid the groundwork for my own.

I also would like to thank Dr. Stefen K. Estreicher, and Dr. R. L. Lichti for serving as my committee members.

I would also like to recognize Dr. John Aidun, Peggy Aragon, and the entire staff in organization 9235 at Sandia National Laboratories. They were exceptionally friendly and helpful to me during my time there. I would also like to thank Dr. Fred Zutavern, Dr. Alan Mar, and Dr. Guillermo Loubriel (three of the members of PCSS experimental team at Sandia National Laboratories) for their encouragement and many helpful conversations about lock-on and PCSS's in general.

CONTENTS

ABSTRACT

In this dissertation, a collective impact ionization approach is used to develop a generalized theory of electrical breakdown in insulators, which includes both the electric field dependence and the carrier density dependence of impact ionization. This theory is applied to photoconductive semiconductor switches (PCSS's) and is used to explain the lock-on effect, an optically triggered breakdown that occurs in GaAs PCSS's. The basic principle of collective impact ionization theory is that, at high carrier densities, carrier-carrier scattering will enhance the impact ionization rate. This occurs because these interactions increase the number of carriers with energies above the impact ionization threshold.

This generalized breakdown theory uses a rate equation approach to find the carrier density or densities which, at a given electric field, result in a steady state or a zero net carrier growth rate. In this approach, the competition between carrier generation (by impact ionization) and carrier recombination (by Auger and defect mechanisms) leads to a steady state condition for the net carrier growth rate. It is the existence of this steady state which governs whether or not electrical breakdown occurs. This approach leads to a definition of the bulk breakdown field as the lowest field for which the injection of an infinitesimally small carrier density will result in a steady state with a large carrier density. It also leads to the definition of the lock-on field as the lowest field for which a stable, steady state carrier density is possible.

To implement this theory for PCSS materials, the Ensemble Monte Carlo (EMC) method is used to calculate the carrier distribution function, including the effects of carrier-carrier scattering. This distribution function is used to calculate the impact ionization and Auger recombination rates and thus the steady state carrier growth rate. Since the EMC calculations which include cc-scattering are computationally intense and time consuming, this theory is also implemented using both low and high density approximations for the distribution function. The low density limit is obtained using the EMC method without including cc-scattering. The high den-

sity limit is obtained by approximating the distribution function as a steady state Maxwellian. Using this theory, predictions are made for both the lock-on field and the bulk breakdown field in several materials and the results are compared, where possible, with experiment.

In this theory, the lock-on effect is a type of carrier-density dependent electrical breakdown which occurs in all insulating materials. Further, it is the difference between the predicted lock-on and the breakdown fields which determines whether or not the lock-on effect will observable as a phenomenon distinct from ordinary breakdown. If the two fields differ by a large amount, it is likely that the two phenomena can be distinguished. However, it they are close to each other, it is likely that they will be difficult to separate experimentally.

LIST OF FIGURES

CHAPTER I
INTRODUCTION

Photoconductive semiconductor switches (PCSS's) are optically triggered solid state switches [1]. In the linear or normal mode, the optical source photogenerates the current carriers, so the opening and closing times for a PCSS depend on the intrinsic properties of the material from which the switch is fabricated, primarily GaAs and Si [2]. Linear mode PCSS's have several advantages for high power switching. These include fast opening and closing times, very low jitter, high repetition rates, and scalability. The major disadvantage for linear mode PCSS's is the large amount of optical energy necessary to close the switch compared to other types of solid state switches. Also, switching in the linear mode requires that the optical source be on continuously for the current to continue to flow, because when the optical source is turned off, the current flow falls quickly to zero due to rapid recombination of the electrons and holes.

In the early years of PCSS development, the desire to make physically smaller switches led to several problems in the fabrication of the switches as well as to the initial observations of a high gain, non-linear switching regime which has been named "lock-on" [3, 4, 5, 6, 7]. This phenomena, which is one of the main focuses of this work, is described in the next paragraphs and is discussed at length in Chapter 3.

When a PCSS operates in the linear mode all (or almost all) of the current carriers come from photo-generation by the optical source. However, for PCSS's made from GaAs or a few other materials, if the initial field across the switch is large enough and the energy of the trigger is high enough, then when the trigger light is turned off, the current will continue to flow in filaments. This state is called the lock-on mode, or more simply lock-on.

In addition to the filamentary current flow, the lock-on mode is primarily characterized by a persistant, or "locked-on" voltage across the switch after the optical trigger is turned off. The lock-on field does not depend on the initial applied field

[4], as long as that field is above the threshold value. The lock-on field is also substantially lower than the intrinsic breakdown field for the material. It is worth noting that both the lock-on field and the threshold field are characteristics of the material from which the switch is made [4], so normally one speaks of the lock-on field and not the lock-on voltage. While the lock-on field is a property of the material itself, it is possible to raise it by irradiating the switch with neutrons [8].

The collective impact ionization theory proposed by Hjalmarson *et al* [9, 10, 11] explains this behavior as a form of high carrier density electrical breakdown. The presence of carrier-carrier (cc) scattering will, at high densities, redistribute the energy of the carriers, eventually resulting in a high temperature Maxwellian distribution. At a given field, this energy redistribution will enhance the high energy tail of the distribution function, increasing the number of carriers above the impact ionization threshold. This will increase the impact ionization rate at that field, allowing breakdown to occur at fields much lower than the intrinsic breakdown field. A proof in principal of this theory has been made by Kang [11].

The original focus of this research was to investigate the lock-on effect in several semiconductors through the application of collective impact ionization theory. However, as the work progressed, it was realized that collective impact ionization theory could not only be used to investigate lock-on but could also be used to investigate the more general problem of electrical breakdown, allowing us to develop a new theoretical approach to this old problem. Three major classes of calculations are performed in this work. 1) Ensemble Monte Carlo (EMC) simulations without carrier-carrier scattering are used to calculate the carrier distribution function at low carrier density. 2) Ensemble Monte Carlo (EMC) simulations including cc-scattering are used when the carrier density is high. 3) At very high carrier density, it is assumed that the carrier distribution function is Maxwellian at a carrier temperature much higher than the lattice temperature. The EMC method including cc-scattering is the most computationally intense of thethree methods and it involves several assumptions and approximations, which are discussed in Chapter 6.

One of the unique approaches in this research is the idea of viewing lock-on in particular and electrical breakdown in general as being defined by a steady state in which the carrier generation and carrier recombination rates are equal. This approach has led us to conclude that lock-on is not a phenomena distinct from intrinsic electrical breakdown, but rather it is an expected consequence of breakdown. This dissertation therefore presents a new, generalized theory of electrical breakdown, in which lock-on is a consequence of the carrier density dependence of electrical breakdown.

This document is organized as follows: Chapter 2 gives an in-depth description of the PCSS's. Following this is a discussion of lock-on in Chapter 3, and a review of electrical breakdown in Chapter 4. Collective impact ionization theory, which forms the basis of this generalized breakdown theory, is discussed in Chapter 5. Chapter 6 discusses in more detail how the calculations, including the Monte Carlo and Ensemble Monte Carlo calculations, were done. Results are presented in Chapter 7, and Chapter 8 contains a summary and some conclusions.

CHAPTER II
PHOTOCONDUCTIVE SEMICONDUCTOR SWITCHES

Photoconductive semiconductor switches (PCSS's) were first developed at Bell labs in 1975 [1]. In the linear mode, a PCSS enters a conductive on state when the surface is illuminated by an optical source, either uniformly or with a laser. It returns to the insulating off state when the source is discontinued. PCSS's made from GaAs and some other direct band gap materials have also shown a type of low field breakdown, the lock-on mode, in which the current flows in filaments. The lock-on mode, one of the primary focuses of this research, is discussed in more detail in Chapter 3. A simple schematic of a typical PCSS with its application circuit is shown in Fig. 2.1. It is worth noting the similarity between a PCSS and an electron beam controlled switch, for which the trigger is an electron beam instead of a optical trigger, since these switches also experience lock-on [12].

There are two major PCSS geometries, "lateral" and "vertical". For a PCSS, the term "lateral" (Figs. 2.2a and 2.1) means that the applied field is perpendicular to the trigger, and "vertical" (Fig. 2.2b) means that the applied field is parallel to the trigger [13]. Most PCSS's designed to operate in the linear mode are lateral switches due to the simplicity of fabricating with this geometry and the longer closing time needed in a vertical switch because the conducting region must go all the way through the material. However, the vertical geometry has been used when the switch will be operated in the high gain or lock-on mode because it is possible to seed the filament near one contact so that it will grow toward the other contact without requiring additional power. The other advantage of vertical switches is that they are not as prone to surface flashover, which is a major disadvantage for lateral switches.

A simple explanation for the standard operation of a lateral PCSS in the linear mode is illustrated schematically in Fig. 2.3. When the optical trigger is shone on the semiconductor surface, it creates a temporary conductive region within the material by activating electrons from the valence bands into the conduction bands. Every

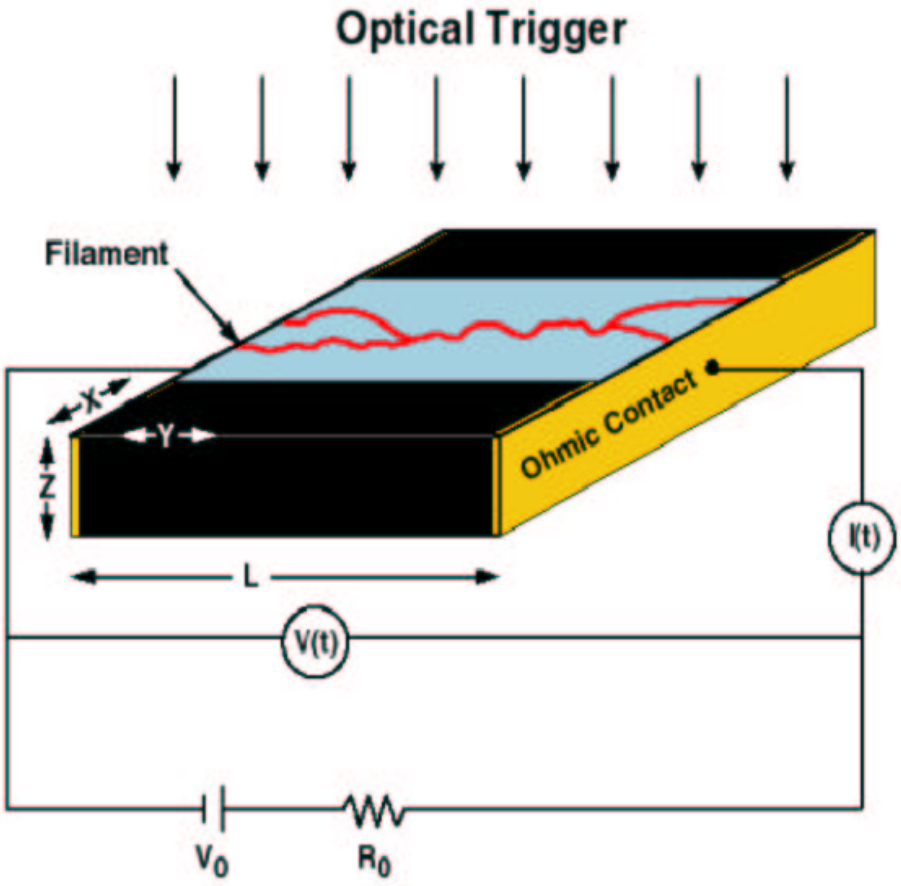

Figure 2.1: A photoconductive semiconductor switch (PCSS) with a simple application circuit.

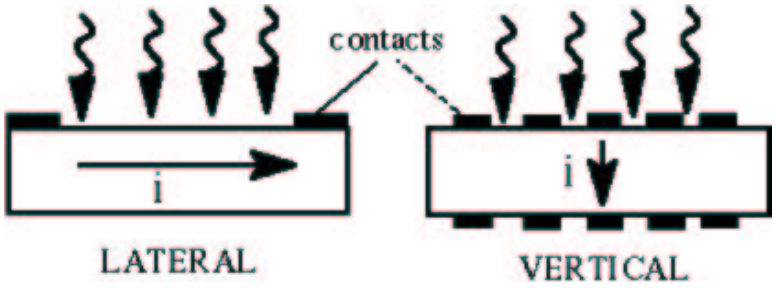

Figure 2.2: A graphical representation of the lateral (a) and vertical (b) geometries for PCSS's.

activated electron leaves behind a hole, which acts as a current carrier. From this simple explanation, it is easy to see that the number of conduction electrons and the

number of holes must be the same and that all of the active carriers come from the optical trigger. A similar argument can be made for a vertical PCSS.

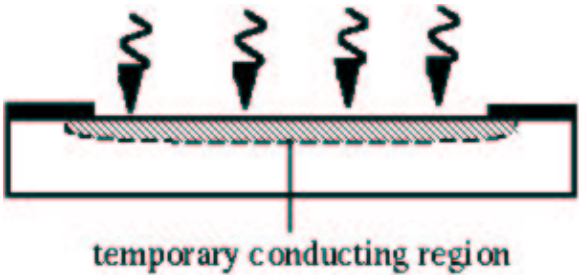

Figure 2.3: A simple view of PCSS operation for the lateral geometry.

As noted in the introduction, the two most common materials used in the fabrication of PCSS's are silicon (Si) and gallium arsenide (GaAs) [2]. Because of its direct band gap, GaAs has a much smaller characteristic recombination time than Si [14]. This makes the opening time of the switch (the time required after optical trigger turn off for the current to stop flowing) much lower for GaAs in comparison with that of Si. GaAs also possesses higher carrier mobilities than Si [14], thus resulting in a higher speed PCSS. It also has a dark resistivity which is several orders of magnitude higher than Si [14], allowing a GaAs PCSS to withstand higher voltages in the off state. Researchers have examined the use of many other materials, including InP, for use in PCSS's but Si and GaAs remain the most commonly used.

The average electric field, F, across a PCSS is defined as $F = V/l$ where V is the voltage drop across the switch and l is the effective length of the device. The resistance of the on state for a PCSS is proportional to l^2/u_0 [15], where u_0 is the incident optical energy. So, from an energy cost perspective it makes sense to shrink the switch as much as possible while keeping the voltage fixed. This shrinkage means switching higher fields, which led to the observation of the lock-on phenomenon in GaAs PCSS's [3, 4, 5, 6, 7].

CHAPTER III
LOCK-ON

Lock-on was first observed by Loubriel, O'Malley, and Zutavern at Sandia National Labs [4, 5], and confirmed at USC [16] and Old Dominion [17]. They were expecting the standard quick carrier recombination and small relaxation time characteristic of PCSS's in the linear or normal mode discussed in the previous chapter. The expected behavior was observed at low fields. However, for electric fields above about 8 kV/cm something unexpected happened. Instead of the current flow stopping when the illumination was discontinued, some current continued to flow and the voltage across the switch dropped to a relatively low, but stable, level. This state was named "lock-on", since the switch is locked on to a sustained voltage. Though occasionally one speaks of the lock-on voltage, it is more common to speak of the lock-on field, because the lock-on field is a property of the switch material, while the voltage depends on the length of the switch.

One of the most intriguing aspects of the lock-on behavior is that, once the initial applied field is greater than the threshold field, the lock-on field does not depend on the initially applied field. This can be seen in Fig. 3.1, which is data taken by Loubriel and Zutavern at Sandia National Laboratories [3].

In a PCSS, once the switch is triggered into the lock-on mode, it and its associated current filaments will continue until either 1) the switch is damaged by the filaments, 2) it is reactivated into the linear mode by triggering, or 3) the field supplied by the power supply drops below the lock-on field. The third possibility occurs because in many PCSS applications the voltage is not supplied by a battery; a capacitor is used instead. As the capacitor discharges, the voltage it is applying to the circuit drops. Since the lock-on field remains constant, the current through the load must fall. This continues until the applied field drops below the lock-on field and current flow ceases.

After the initial observations of lock-on there was both experimental and theoretical interest in further defining its properties, including the temperature dependence

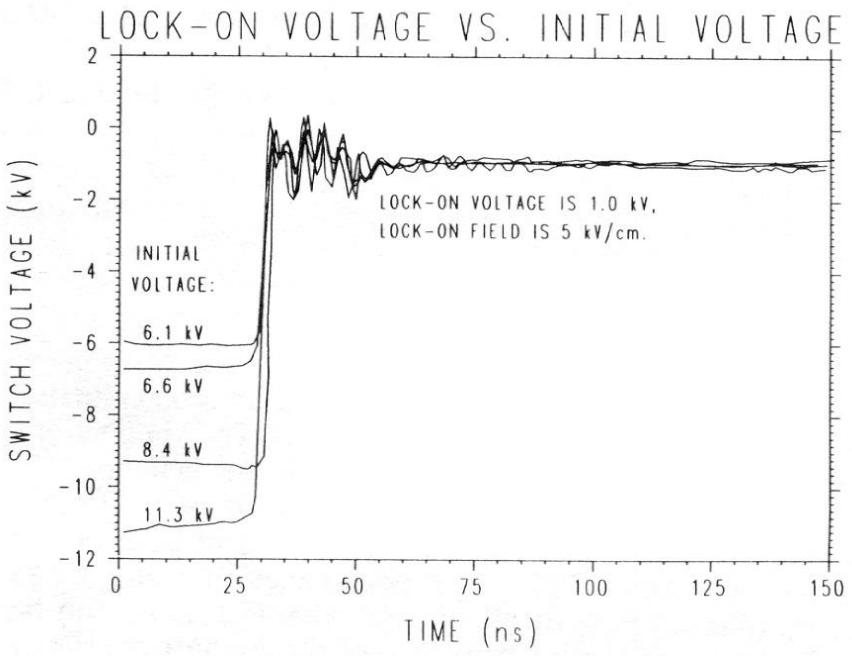

Figure 3.1: Experimental observation of lock-on in a GaAs PCSS. Time dependence of switched voltage in a 2 mm long switch [3].

of the lock-on field (the lock-on field decreases when the temperature decreases [18]) and its dependence on the impurity concentration (the lock-on field increases in GaAs with increasing Cr concentration [18]). However, probably the most important experimental result was the observation of filamentary current flow in 1991 [19, 20]. The current filaments are somewhat analogous to lightning passing through the material. The filament, of a GaAs PCSS, produces light in the infrared range due to GaAs 1.4 eV band gap. An infrared photograph [8] of such a filament is shown in Fig. 3.2. Both the number and placement of these current filaments can be controlled by carefully adjusting the trigger laser [21, 22]. Furthermore, a filament laser has been developed at Sandia National Laboratories [23].

Considerable effort has been expended looking for lock-on in other materials besides GaAs. Among these are Si, in which it has yet to be observed, and InP in which it has [3, 18, 24, 25]. Because GaAs and InP are both III-V materials with large

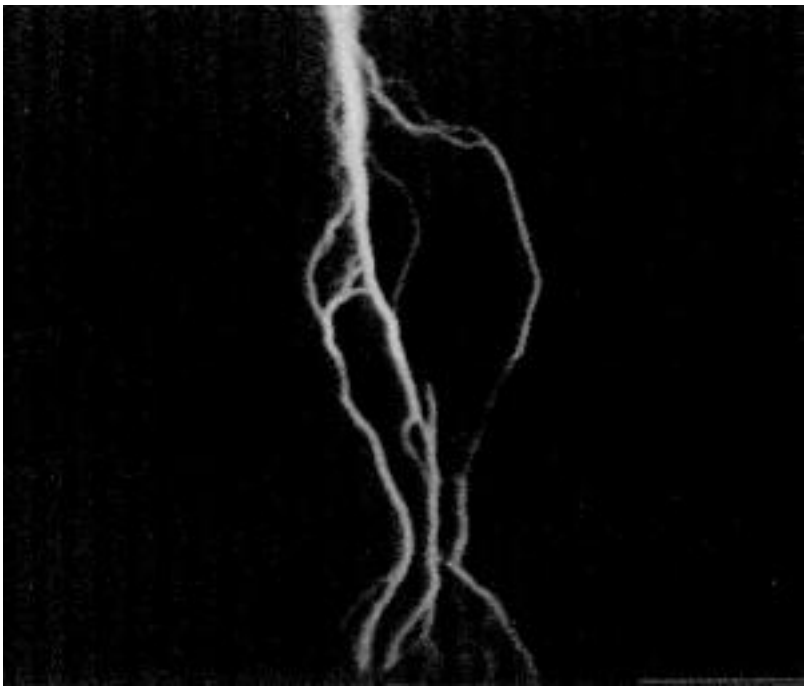

Figure 3.2: An infrared photograph of a lock-on current filament in GaAs [8].

direct band gaps, an effort was also made to determine if GaP would show evidence of lock-on. Since GaP has an indirect band gap but is otherwise very similar to GaAs and InP the fact that lock-on was not observed helped to confirm the idea that it seems to be limited to materials with direct band gap zinc-blende bandstructures [26]. The only experimental observation of lock-on in an indirect gap material was in a diamond electron beam switch in which a lock-on field of 0.8 MV/cm [27] was observed.

For most applications lock-on has advantages. One advantage of the lock-on state is that the optical trigger energy required to initiate it is approximately .1% of the optical energy required to initially activate the switch from an off state to the linear on state [19]. For this reason, one of the primary focuses of the experimental work has been to limit the damage caused by the filaments at the electrical contacts. This damage is the main failure mechanism for the switches [21, 22, 28, 29, 30, 31]. This work has included redesigning the contacts [21, 28, 30, 32, 31, 33, 34], using multiple

current filaments to distribute the current density [34, 35], and triggering the PCSS in such a way as to minimize the damage [29, 31].

It is possible to open a switch that is in the lock-on mode if the switch material has been doped with deep-level impurities. In this case a second laser pulse is used to quench the switch out of the lock-on mode [36]. When combined with the advantage of the energy saved by triggering into the lock-on mode, this allows the creation of a bulk optically controlled semiconductor switch (BOSS) in which one laser pulse closes the switch and then another pulse opens the switch again [36, 37, 38].

3.1 Theoretical Explanations for Lock-on

Several theories have been proposed to explain the lock-on effect. Among such theoretical explanations are metastable impact ionization [39], double injection and carrier trapping [40, 41, 42], avalanche injection [43, 44], localized impact ionization [45], and collective impact ionization [9, 10].

Metastable impact ionization theory proposes that the lock-on effect comes from the ionization of deep traps, as opposed to traditional band-to-band impact ionization [39]. This method would lower the necessary field for breakdown, since ionizing traps requires less energy than ionizing carriers directly from the valence band. Although this theory properly predicts a lock-on field independent of switch size, metastable impact ionization also predicts that one can cause lock-on to occur without any optical or electron beam triggering, which is not in agreement with experiment. In fact an untriggered GaAs:Cr PCSS withstood an applied electric field of 16.8 kV/cm for 30 minutes without entering lock-on [3].

Double injection theory proposes that carriers are injected into the material from the contacts [40, 41, 42]. At low voltages most of these carriers are trapped near the contacts by deep levels and, as the field increases, they penetrate deeper into the material. Once all of the traps are filled, recombination becomes slow and the carriers that remain carry the lock-on current. According to this theory, this does not happen to the bulk without the optical trigger is because there are many traps and

the injected carriers are too small in number to fill them all. However, if one injects many carriers optically, then the traps are quickly filled.

The proponents of avalanche injection theory noted that many PCSS's use n-doped contacts for both the anode and the cathode and that the anode contact will not therefore inject holes [43, 44]. Instead, these holes come from the formation of a static Gunn domain at the anodethat creates a high field region in which impact ionization occurs, thus injecting holes into the undoped switch.

Both of these theories reproduce some of the basic lock-on behavior. However the speed of propagation of any filaments based on on either of these theories would be at most the carrier saturation drift velocity. On the other hand, the measured speed of the current filaments during formation is over 100 times larger than the saturation velocity in GaAs [46, 47].

Localized impact ionization theory works by assuming that at some point on a contact there is a defect of some kind which enhances the field at that point to such an extent as to begin impact ionization [45]. It then treats conduction within the filament and outside the filament in separate 1-D calculations. This model also fails to predict the correct speed of filament propagation. Perhaps more importantly, it also predicts that the filament will originate at the non-illuminated contact. However experiments show the opposite to be true [46, 47].

Finally, there is the collective impact ionization theory [9, 10], which is the basis for this research and which is discussed in detail in Chapter 5. One principle of this theory is that lock-on is not a unique phenomena but is a special case of carrier density dependent electrical breakdown. In subsequent chapters, it is shown that lock-on occurs if the trigger injects enough carriers so that carrier-carrier interactions significantly enhances the impact ionization rate. This enhancement allows breakdown to occur at fields much lower than the intrinsic breakdown field.

CHAPTER IV
ELECTRICAL BREAKDOWN

As has been discussed, this theory proposes that the lock-on effect is an aspect of electrical breakdown. Further, the calculations discussed in subsequent chapters help to confirm this. Therefore, it is worthwhile to briefly review previous approaches to the old problem of electrical breakdown in insulators. Since this problem is very old, many researchers have made contributions to it. So, rather than give an exhaustive review of this area, here the major theoretical approaches which have been taken are outlined. From an experimental viewpoint, breakdown is primarily characterized by a sudden increase in the carrier density when the applied field reaches the breakdown field. The primary difference between electrical breakdown, the focus of this chapter, and thermal breakdown is that thermal breakdown also involves heating of the lattice not only of the carriers. Thermal breakdown is caused by changes in the physical properties of the material as the temperature rises. On the other hand, electrical breakdown occurs at much lower temperatures and is controlled by the electrical properties of the device [48]. It is not unusual for electrical breakdown to occur, thus raising the temperature of the sample and leading to the onset of thermal breakdown.

4.1 Impact Ionization

There are two major classes of electrical breakdown theories, intrinsic breakdown theory and avalanche breakdown theory [48]. Both classes focus on impact ionization as the carrier generation mechanism; therefore, to understand them, it is first necessary to understand what is meant by impact ionization.

Impact ionization is a specific type of carrier-carrier scattering in which an electron high in a conduction band collides with an electron in the valence band. This promotes the second electron into the conduction band. At the same time, the electron initially high in the conduction band drops to a lower energy, also in a conduction band. It is, of course, necessary that energy and momentum are conserved. After an impact

ionization event, there are two new carriers, an electron in the conduction band and a hole in the valence band. A schematic diagram of an impact ionization event for parabolic bands is schematically shown in Fig. 4.1.

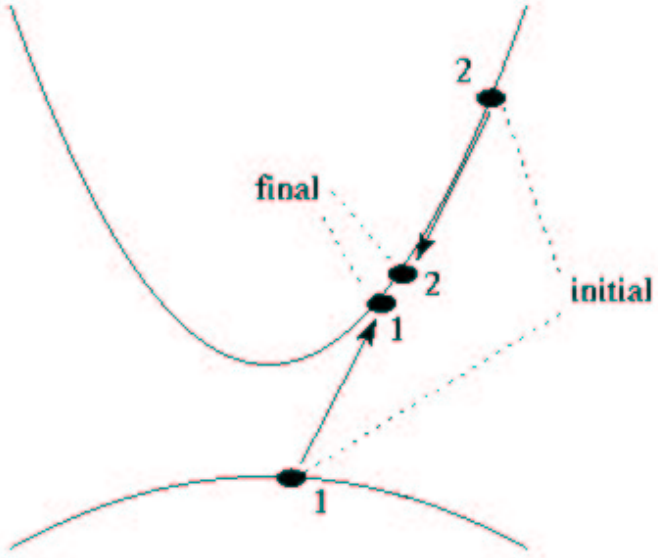

Figure 4.1: An example of an impact ionization scattering event for parabolic bands.

Since most semiconductors have bandgaps of at least 1 eV, this means that the high energy electron which initiates impact ionization must be at least 1 eV above the conduction band minimum. The need for such a high energy electron means that it is the high energy tail of the electron distribution function which controls the impact ionization rate. Therefore, that rate is usually low except at very high fields.

4.2 Intrinsic Breakdown

In intrinsic breakdown theory [49, 50, 51, 52, 53] breakdown occurs if the average carrier energy exceeds a threshold for impact ionization. Thus it occurs of the carriers become too "hot" independent of the lattice temperature. This impact ionization then creates more and more carriers and breakdown eventually occurs.

Though there are several different criteria for determining when breakdown is reached, the fundamental idea of each is the same. A carrier with energy E will gain energy from the field F at a rate, $A(F,T,E)$, and it will lose energy to the phonons at a rate, $B(E,T)$. In these expressions T is the lattice temperature, which is not necessarily the same is the carrier temperature T_c [53]. Fröhlich showed that for high energy carriers while the heating rate A increases proportionally to $E^{3/2}$, but the cooling rate B depends on $E^{-1/2}$ [51]. Using the notation of O'Dwyer [48], this means that for a given field there is an energy E' such that

$$A(F,T,E') = B(E',T). \tag{4.1}$$

Any carrier with an energy above E' will gain more energy from the field then it will lose to the lattice. The two criterions both use this idea, the difference is what energy is used for E'.

The Fröhlich criterion uses the idea that one finds the breakdown field by determing the field for which E' is the ionization energy, usually approximately the same as the band gap E_g. So, the breakdown field F_B is defined as the field for which

$$A(F_B,T,E_g) = B(E_g,T) \tag{4.2}$$

The logic for this criterion is fairly simple. Once an electron has the energy needed to impact ionize then, it will, on the average, either gain energy or stay at the same energy until it does so. This is true whether that high energy electron comes from field heating or from a recombination event. Since the high energy electrons created by Auger events will not cool but instead stay at high energy, there will be more impact ionization than Auger recombination for fields at or above the breakdown field.

Another breakdown criterion used is the Von Hippel-Callen criterion [49, 50]. As noted above, for high energies the cooling rate decreases as a function of carrier energy, but at low energies it is an increasing function of energy. This means there

is an energy for which the phonon cooling is a maximum. The Von Hippel-Callen criterion uses this maximum cooling energy in Eq. 4.1 to define the breakdown field. This guarantees that the Joule heating rate, the rate at which the carriers gain energy from the field, will always be larger than the phonon cooling rate, the rate at which phonons remove energy from the carriers. Thus, on average, carriers at all energies will gain energy and will eventually reach the impact ionization threshold.

In intrinsic breakdown theories, the separation of the contacts is not considered. Effectively, this means that a large sample is assumed. The breakdown field is described as the intrinsic breakdown field because the breakdown field depends only on the material itself not on the contact separation or the geometry of the switch. Intrinsic breakdown theories are used primarily to explain breakdown in dielectric materials including alkali halides, glasses, and mica [48]. Though this method and theory are significantly different from the intrinsic breakdown theories discussed above there are common points. First, this theory shares the assumption of a large sample length, necessary for EMC calculations. Second, this theory also bases the breakdown field of a device strictly on the properties of material, not the contacts. For these reasons, it is a theory in the class of intrinsic breakdown.

4.3 Avalanche Breakdown

Avalanche breakdown theories are usually used to explain the breakdown of p-n junctions. In avalanche theories, the separation of the electrodes determines the junction's breakdown field. In the case of avalanche breakdown, the breakdown field is based on how much carrier multiplication will occur in the time it takes for the electron to travel between the electrodes. If the junction is thin enough, field-emission avalanche breakdown may occur.

Much of avalanche breakdown theory is similar to the theory of breakdown of insulating gases. In avalanche theories, electrons are heated by the field between the contacts and are cooled by the phonons as they move through the material. Once an electron reaches a high enough energy it will impact ionize, producing an additional

electron. The two low energy electrons then begin the process over again. If the field is high enough, it will push those low energy electrons back up into the high energy region and they will impact ionize again, producing more electrons, and so on resulting in an "avalanche" of electrons [48, 54, 55].

According to this theory there will be 2^i electrons after the i-th generation. Assuming that it begins with one electron, if there is only enough time before the electron reaches the other contact for the number of electrons to increase to 8 ($i = 3$), then clearly that will not cause a large increase in current corresponding to breakdown. For breakdown to occur, there must be a large number electrons created by impact ionization for each electron injected. Normally, the value of i chosen to represent breakdown is around $i = 40$ [48]. The value is from an approximate analysis by Seitz [54]. In his analysis, he assumes a breakdown field on the order of 1000 kV/cm and a mobility on the order of 1 $cm^2V^{-1}s^{-1}$. This means that, in 1 μs the electron would travel approximately $1cm$ in the direction of the field. During the same time wanders in a plane parallel to the field. This wandering is governed by the diffusion coefficient which is assumed to be 1 cm^2s^{-1}. So the electron will wander, perpendicularly to the field, a maximum of $\approx 10^{-3}$ cm. These distances can be used to define a cylinder which has about 10^{17} atoms which could be disrupted by an energy of order 10 eV per atom. Given the assumed field, this would require about 10^{17} electrons. Setting $10^{17} = 2^i$ gives about 40 generations [48, 54]. Thus, according to this approach, the question becomes would a single electron leaving one contact be able to undergo 40 impact ionization events before reaching the other contact? If it can, then breakdown occurs. If it can not, either because the field is too low or the the contacts are too close together, then breakdown does not occur. It is worth noting that this theory predicts that an infinite sample will have an infinitesimal breakdown field.

CHAPTER V
COLLECTIVE IMPACT IONIZATION

Collective impact ionization theory has been proposed by Hjalmarson *et al.* [9, 10, 11] to explain lock-on, and it explains most of the characteristics of this phenomenon. This theory is based on a unique band-to-band impact ionization mechanism in which impact ionization becomes increasingly more efficient as the carrier density increases, due to carrier-carrier interactions. This idea was initially proposed to explain lock-on. However, as described below and in later chapters, it can be generalized to develop a new theory of intrinsic electrical breakdown. This discussion will begin using the collective impact ionization idea to qualitatively explain lock-on and then will move toward describing what it implies about a general theory of intrinsic breakdown.

5.1 S-like current-voltage characteristic

To explain the lock-on phenomenon, the guiding assumption of collective impact ionization theory is that a PCSS acts as a bistable switch. This implies that it has an S-like current-voltage (IV) characteristic, as shown schematically in Fig. 5.1. Such a characteristic is required for the stable filamentary current flow that has been observed experimentally during lock-on [19]. In addition to the S-like IV curve, Fig. 5.1 also shows the load line of the circuit attached to the switch. The load line assumes a resistive circuit. Because the voltage being plotted is the voltage across the switch, not the resistor, the load line has a negative slope. The three points of interest are the intersections of the load line and the IV curve. The low current point is the "off" state of the switch corresponding to the switch before optical triggering, and the high current point is the "on" state corresponding to lock-on. Both of these solutions are stable states. The third point, in the middle represents an unstable state for the switch. Figure 5.1 also predicts a lock-on threshold voltage since there are load lines which could be drawn that would not have two steady states.

It is worth noting that the linear mode is not actually shown on the IV curve in

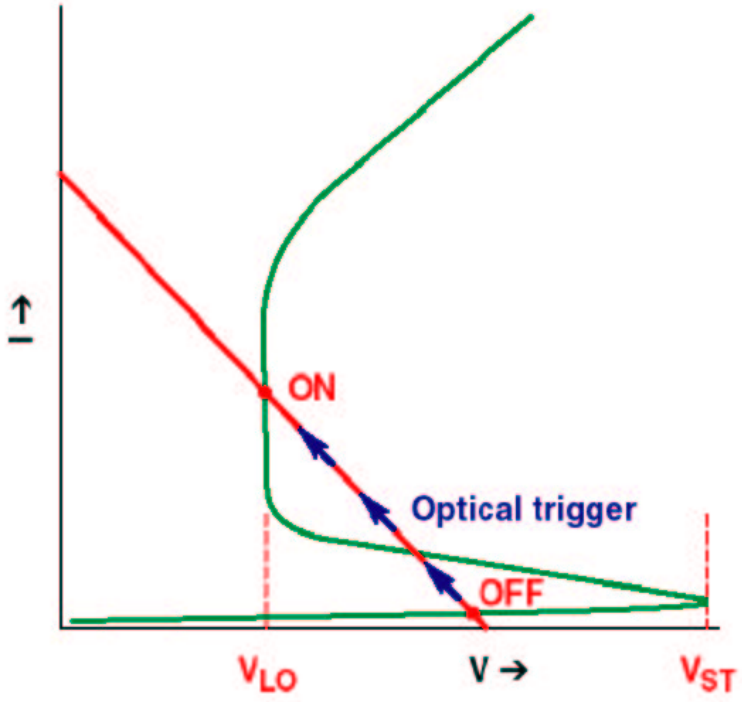

Figure 5.1: A schematic of the S-like current-voltage curve in a PCSS.

Fig. 5.1, since it involves the constant injection of carriers. One could think of the linear mode as being near the zero voltage/high current extreme of the load line. In fact, it may be easier to understand this figure if one thinks of it in terms of the direct triggering into the lock-on mode. First, the voltage and the resistance are connected to the PCSS and the system is in the off state. Then, the optical injection is started, increasing the carrier density in the switch, and current begins to flow. This current flow causes the voltage across the PCSS to drop. The relationship between the current and the voltage follows the load line, and if the injected carrier density is high enough (or put another way, if the trigger energy is high enough) then the switch reaches the second stable state, the lock-on state. For this reason, the graph shows the optical trigger driving the system up the load line from the "off" state to the "on" state. A question which could be asked is what happens if the switch is triggered into the linear mode first? In this case, the trigger also causes the system to move up the

load line, only in this case it continues up into the high current low voltage extreme. When the trigger is discontinued the system comes back down the load line and stops at the lock-on steady state.

Thus Figure 5.1 shows that the S-like IV curve of a PCSS predicts both a threshold field and a threshold trigger energy for the lock-on state and that it also predicts filamentary current flow.

5.2 Carrier-Carrier Scattering

An S-like IV curve can be produced if the impact ionization coefficient depends on the carrier density. The inclusion of carrier-carrier(cc) scattering, as assumed in collective impact ionization theory, means that when two hot carriers scatter with each other, one gains energy and the other loses it. These interactions alter the distribution function, enhancing the high energy tail. For high enough carrier densities, the distribution function becomes a Maxwellian, described by an effective carrier temperature. This redistribution creates more carriers with high enough energy to undergo impact ionization. This is shown schematically in Fig. 5.2.

Figure 5.2 is a schematic plot of the electron distribution function in GaAs, on a log scale, as function of the electron energy. The energy gap, E_{gap}, is shown as a vertical line on the graph and is the minimum energy required to impact ionize. (The actual minimum energy required for impact ionization, or the impact ionization threshold energy, is slightly higher than the energy gap because of the need for momentum as well as energy conservation.) The impact ionization rate will depend on the fraction of carriers with energy above E_{gap}. The single particle, or low density, curve shows a two temperature distribution function with very few high energy electrons. This occurs because, for energies below the L point energy, $E_{\Gamma L}$, the distribution function is largely controlled by polar optical scattering, but above $E_{\Gamma L}$ the distribution function is effected by optical and acoustic deformation potential scattering [11, 56]. However, the collective, or high density, curve has a single temperature resulting in far more high energy carriers.

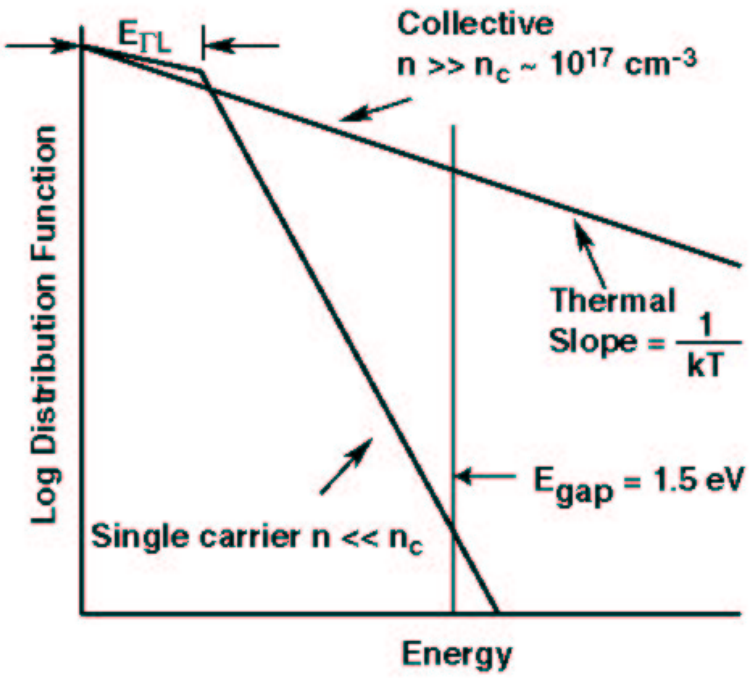

Figure 5.2: A schematic of the carrier distribution function illustrating the collective impact ionization concept in GaAs.

Using this fact, the schematic carrier distribution function plot in Figure 5.2 can be used to help predict when lock-on will be observed experimentally and when it will be difficult to observe. If the distribution function without cc-scattering is already nearly Maxwellian then including the effect of cc-scattering will not create major differences in either the distribution function or the impact ionization rate. This implies that the lock-on and breakdown fields will be close to one another, and differentiating them experimentally would be difficult. However, if the distribution without cc-scattering is very non-Maxwellian, then the effects of carrier-carrier (cc) scattering on the distribution function and the impact ionization rate will be larger. This implies the lock-on and breakdown fields will be further apart. In this case lock-on should easier to observe experimentally.

Figure 5.2 also qualitatively explains the filamentary nature of the lock-on current.

Inside the filament the high carrier density produces a high cc-scattering rate, which enhances the high energy tail of the distribution function. This produces more impact ionization, which helps to maintain the high carrier density. Outside the filament there is a low carrier density, and without the enhancement caused by carrier-carrier scattering, the field is simply too low to produce a significant number of high energy carriers. Thus the simultaneous existence of high and low density steady states allows for a stable current filament to exist.

5.3 Rate equation method

The approach used in this work is to calculate the field and carrier density dependent rate of change of carrier density, defined as the difference between the carrier generation and recombination processes. This approach uses steady state solutions to model breakdown and it is assumed that the only means of carrier generation is impact ionization. Two types of recombination are included, Auger recombination and recombination at defect centers.

The rate of change of carrier density, $\frac{dn}{dt}$, including these three processes, can be written as

$$\frac{dn}{dt} = \int f_k(r_{ii} - r_{Auger} - r_{defects})d^3k \tag{5.1}$$

in which the integral is over the Brillouin zone and where r_{ii}, r_{Auger}, and $r_{defects}$ are the impact ionization, Auger, and defect recombination rates respectively and f_k is the k-space distribution function. The impact ionization and Auger rates can be readily tabulated as a function of wavevector, and in this analysis the defect recombination is assumed to be equal to a constant r times the carrier density. This means that the main goal of this research is to calculate the distribution function to be used in Eq. 5.1.

Before beginning the actual calculations, it is worth while to obtain conceptual insight using well known information and approximations. Since the approximate forms of the three rates in Eq. 5.1 are known [48, 57], it is possible to write an

approximate expression for the rate of change of carrier density as a function of carrier density. It has the form

$$\frac{dn}{dt} = Rn = C(F,n)n - an^3 - rn, \tag{5.2}$$

where $C(F,n)$ is the impact ionization rate coefficient, a is the Auger rate coefficient, and r is the defect recombination rate coefficient. The situation of primary interest is the behavior when the carriers are in a steady state. Thus the goal becomes finding the conditions for which $\frac{dn}{dt} = 0$. Obviously when $n = 0$ then $\frac{dn}{dt} = 0$, which makes sense conceptually because there must first be electrons in the conduction band for impact ionization or Auger recombination to occur. The more interesting case is when

$$R(F,n) = C(F,n) - an^2 - r = 0. \tag{5.3}$$

While it is computationally intense to calculate the impact ionization and Auger rates for any real material, it is possible to gain some conceptual insight into the physics of the steady state condition defined by Eq. 5.3 by using established analytical forms to look at the basic behavior. In order to simplify this discussion of the schematic analysis, and the results for the material calculations discussed in Chapter 7, it is assumed that the field across the switch does not change as the carrier density changes. This is essentially the same as assuming a very low resistance load in Figure 2.1. In all real setups of course, increasing the carrier density will increase the current, and this will cause the field across the switch to decrease.

5.4 Schematic Analysis Without Carrier-Carrier Scattering

First, the case for which there is no carrier-carrier scattering is analyzed. For this case, $R(F,n) = R_0(F,n)$ and the impact ionization rate coefficient can be assumed to have the usual empirical form $C(F,n) = C(F) = \alpha_0 e^{-\beta/F}$ (where α and β are constants) [58, 59]. The carrier density for which $R_0(F,n) = 0$ can readily be found using Eq. 5.3:

$$n = \sqrt{\frac{\alpha_0 e^{-\beta/F} - r}{a}}. \tag{5.4}$$

Assuming reasonable values for all phenomenological constants, the carrier density from Eq. 5.4 can be plotted as a function of field. Such a plot is shown schematically as the dashed curve in Fig. 5.3. The intrinsic breakdown field, F_B, is defined as the the lowest field for which there is a real n that makes $R_0 = 0$. This field follows from $\alpha_0 e^{-\beta/F_B} = r$. The curve divides the possible carrier density and field values into three groups. The region below the curve represents carrier densities and fields for which there is a positive rate of change of carrier density. Thus at a fixed field F, if the carrier density n in this region, then the carrier density will increase until it reaches the steady state defined by the curve. The region above the curve represents the densities and fields for which there is a negative rate of change of carrier density. Thus at a fixed field F, if the carrier density n in this region, then the carrier density will decrease until it reaches a steady state. If the field is below F_B then the density

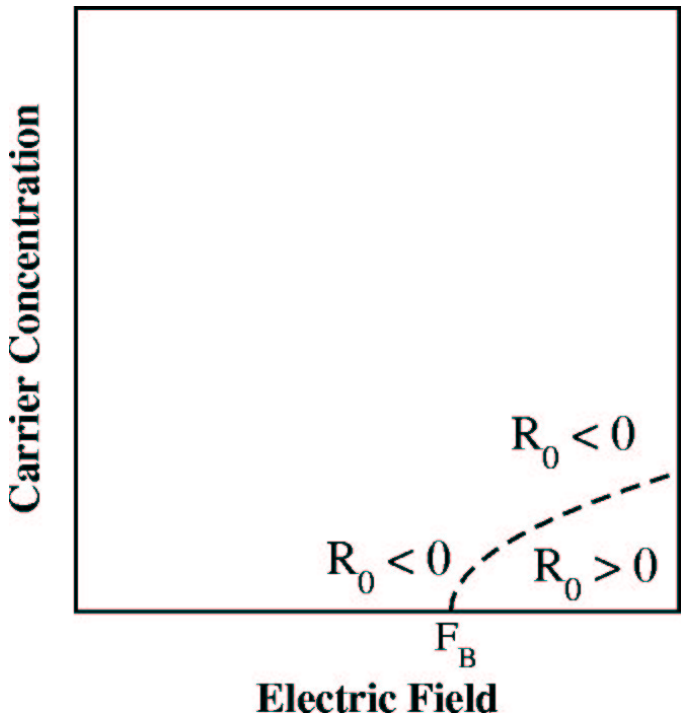

Figure 5.3: A schematic breakdown plot excluding carrier-carrier scattering.

will fall to the steady state at $n = 0$, otherwise the density will fall until it reaches the steady state defined by Eq. 5.4. The third group are those densities and fields which are in steady state and the carrier density will neither grow nor shrink. This is the result given by Eq. 5.4 and is the dashed curve in Fig. 5.3.

Looking at Fig. 5.3, one can see that the steady state solutions are $n = 0$ and then the values as one moves up along the dashed curve defined by Eq. 5.4. For $F \leq F_B$ the $n = 0$ steady state is the only stable steady state since if a few carriers are created, the rate of change of carrier density will be negative and cause the density to decrease to zero. On the other hand, if $F > F_B$, the $n = 0$ steady state is no longer a stable state because if a few carriers are injected the rate of change of carrier density will be positive and n will rise until it reaches the steady state curve defined by Eq. 5.4. The curve represents stable states because if the carrier density were to fall below the curve, then the rate of change of carrier density would be positive. If n were to rise above the curve, the rate of change of carrier density would be negative.

5.5 Schematic Analysis With Carrier-Carrier Scattering

If there is a high carrier density then the n dependence of the impact ionization rate coefficient must be included. For this qualitative discussion only, it is assumed that this will, in a first order approximation, cause $C(F, n)$ to have the form $C(F, n) = \alpha_0 e^{-\beta/F}(1 + \frac{n}{n_0})$ where n_0 is a constant. For the microscopic physics calculations, which are discussed in Chapter 8, this assumption is not used. Though solving Eq. 5.3 is now more difficult, it is still possible to calculate the steady state solutions numerically. This allows us to plot the carrier density as a function of field including the effects of carrier-carrier scattering. The results including cc-scattering are shown schematically as the solid curve in Fig. 5.4. For easy comparison, the dashed curve in Fig. 5.4 shows the results without cc-scattering.

One of the more important things to notice when comparing the results with and without cc-scattering is that the results including cc-scattering actually represent a more traditional form of breakdown. When $F = F_B$, a small injection of carriers

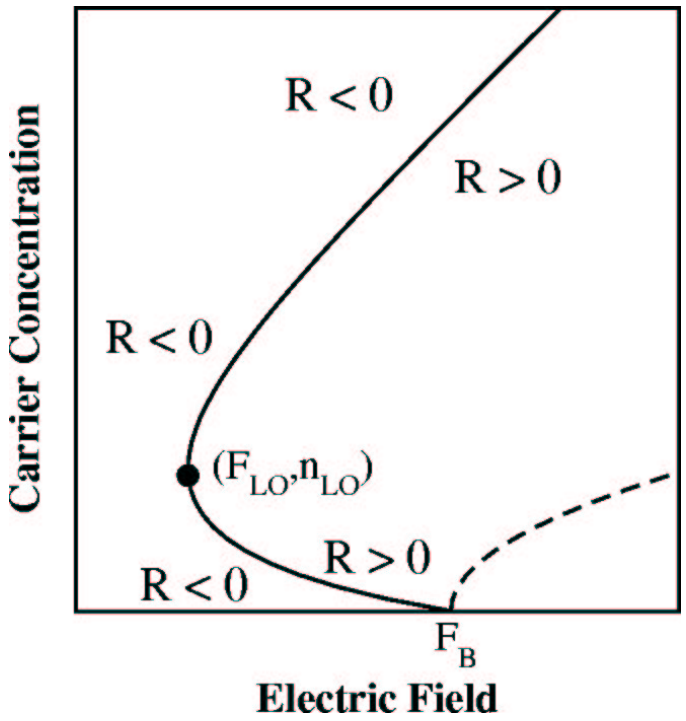

Figure 5.4: A schematic breakdown plot including carrier-carrier scattering.

will result in the creation of a large number of carriers through impact ionization. This process will continue until a steady state is achieved. The calculations with cc-scattering included show that in order for there to be a sudden increase in steady state carrier density at the breakdown field, the impact ionization rate must be dependent on carrier density though not necessarily through collective impact ionization. This result, including the S-like shape of carrier density n as a function of field F, is similar to work done on filamentary gaseous breakdown by Davydov [60].

It is also important to note that the intrinsic breakdown field is the same both with and without carrier-carrier scattering. What is different from the case with no cc-scattering is that when carrier-carrier scattering is included, a form of breakdown can be initiated by injecting carriers into the material at a field lower than the intrinsic breakdown field. The minimum field for which this holds true is defined as the lock-on field, labeled F_{LO} in Figure 5.4.

The solid curve in Fig. 5.4 also shows an S-like behavior similar to Fig. 5.1.

The $n = 0$ steady state is stable until $F = F_B$. If $F < F_B$, the lower carrier density associated with each field represents an unstable steady state because a minor fluctuation in the carrier density will cause the carrier density to either fall to zero or rise to the higher value. However, the higher density for each field is a stable state.

Does an S-like carrier density versus field characteristic, imply an S-like IV curve? To answer this question, remember that the field is the voltage divided by the length of the switch and that the carrier density times the drift velocity is equal to the current density, the current divided by the cross sectional area of the current flow. Of these quantities, only the drift velocity varies with the field, and for most of the voltages of interest in a PCSS the drift velocity will be near the saturation drift velocity, and thus will depend only weakly on the field. Thus the field dependence of the drift velocity will not significantly alter the basic S-like qualitative behavior, and an S-like IV characteristic can therefore be inferred from Figure 5.4.

This implementation of collective impact ionization theory, in an analytic approximation, predicts a bistable switching behavior with a low field electrical breakdown which occurs only when the carrier density is high. That is, it predicts lock-on and allows us to define the theoretical lock-on field as the lowest field for which there is a non-zero carrier density that results in a steady state. It also allows us to theoretically define the intrinsic breakdown field as the lowest field for which the injection of a small number of carriers will result in a steady state with a much larger number of carriers.

While this phenomenalogical analysis offers some insight, it is clear that by choosing different values for the constants will significantly alter the plots, including making the lock-on field nearly identical to the breakdown field. Thus, it is necessary to calculate these constants in a more rigorous way. This necessity leads us to the use of ensemble Monte Carlo methods.

CHAPTER VI
COMPUTATIONAL DETAILS

The approximate analysis done in the previous chapter results in a qualitative explanation of both lock-on and intrinsic breakdown. For a more realistic treatment, three types of calculations are preformed: 1) Ensemble Monte Carlo (EMC) simulations without carrier-carrier (cc) scattering, 2) Ensemble Monte Carlo simulations which include cc-scattering and 3) calculations assuming a Maxwellian carrier distribution. The specifics of these calculations are discussed in this Chapter. In the first two subsections, the single particle Monte Carlo (MC) and EMC methods are discussed in general. For a more detailed discussion see the previous work by Kang[11]. The EMC calculations without cc-scattering method is used to calculate the distribution function solutions to the Boltzmann transport equation for electrons and holes under the influence of an external field without cc-scattering. The EMC method including cc-scattering is used to calculate approximate distribution function solutions to the Boltzmann transport equation for electrons and holes under the influence of an external field including cc-scattering. From these distribution functions along with the quantum mechanical carrier-phonon and carrier-carrier scattering rates, the impact ionization and Auger recombination rates are calculated. The specifics of the Ensemble Monte Carlo calculations done for this work are discussed in Section 6.3. The impact ionization events table is discussed in Section 6.4, and the Maxwellian calculations are discussed in Section 6.5.

6.1 Single Particle Monte Carlo

The MC method divides the motion of a charge carrier in an electric field into two parts: 1) the drift of the electron due to the electric field, and 2) the interaction of the electron with the phonons or other scattering mechanisms.

The motion of the electron in the electric field can be simulated by

$$\vec{k} = \vec{k_0} - \frac{e\vec{F}\tau}{\hbar}, \tag{6.1}$$

where $\vec{k}$ is the final wavevector, $\vec{k_0}$ is the initial wavevector, τ is the time of free flight, and $\vec{F}$ is the electric field.

The other process affecting the electron motion is the scattering by phonons and other scattering mechanisms. In the MC formalism, the scattering mechanisms can change both the magnitude and the direction of the wavevector. This is accomplished by calculating probability of such scattering. The probability that an electron in the state labelled by wavevector k, at time t scatters within the time interval Δt after t is given by [61]

$$P(t)\Delta t = \lambda(\vec{k})e^{-\lambda(\vec{k})t}\Delta t, \tag{6.2}$$

where $\lambda(\vec{k})$ is the total scattering probability per unit time for an electron in that state. If there are several different scattering mechanisms, each with a different scattering probability per unit time $\lambda_i(\vec{k})$, then the total scattering probability $\lambda(\vec{k})$ is

$$\lambda(\vec{k}) = \sum_{i=1}^{n} \lambda_i(\vec{k}). \tag{6.3}$$

Each scattering probability, $\lambda_i(\vec{k})$, can be written as a sum over the possible final states. This means

$$\lambda_i(\vec{k}) = \sum_{\vec{k'}} S_i(\vec{k}, \vec{k'}), \tag{6.4}$$

where $S_i(\vec{k}, \vec{k'})$ is the quantum mechanical scattering rate for process i to scatter an electron from state $\vec{k}$ to state $\vec{k'}$.

The time of free flight can be calculated from a probability distribution by using a random number, γ, which is between zero and one, by use of [62]

$$\gamma = \int_0^{\tau} dt' P(t'). \tag{6.5}$$

In addition to the real scattering, Rees [63] introduced the concept of virtual scattering. Virtual scattering does not represent a physical process, but is very useful as a mathematical tool to simplify the calculations. A virtual scattering event does not change the wavevector or anything else, and has the rate

$$S_i(\vec{k}, \vec{k}') = \frac{2\pi^3}{V}\lambda_0(\vec{k})\delta_{\vec{k},\vec{k}'}. \tag{6.6}$$

where V is lattice volume and $\lambda_0(\vec{k})$ is completely arbitrary.

Combining both virtual and real scattering processes, the scattering probability becomes

$$P(t) = [\lambda_0(\vec{k}) + \lambda(\vec{k})]e^{-\int_0^t dt'[\lambda_0(\vec{k})+\lambda(\vec{k})]} = \Gamma e^{-\Gamma t}. \tag{6.7}$$

where $\Gamma = \lambda_0(\vec{k}) + \lambda(\vec{k})$ and is assumed to be time independent.

By combining Eq. 6.5 and Eq. 6.7, the time of free flight can be shown to be

$$\tau = -\frac{1}{\Gamma} ln(1-\gamma). \tag{6.8}$$

A MC simulation can be broken into steps as follows:

1) The total number of free flights in the simulation is selected. This number should be large enough that the initial conditions do not effect the final distribution, but short enough so as not to waste computational time.

2) The value of Γ along with other parameters, including those governing the scattering rates, are defined. Γ needs to be larger than the total scattering rate, but if it is too large then there will basically be only virtual scattering and the simulation will be useless. The choice of Γ and the number of flights are both balancing acts, and a bad choice of either or both can cause the calculation to be a waste of time.

3) A random number is selected to define the time of free flight for the particle using Eq. 6.8.

4) Using the time of free flight from step 2), the electrons new momentum vector is calculated according to Eq. 6.1 and its new energy is found based on that wave

vector.

5) After the time of free flight, another random number is selected.

6) The electron-phonon scattering rates, as well as the rates for all other allowed types of scattering, are calculated. The random number from step 5) is used to determine which, if any, type of scattering occurs.

7) The wave vector and energy of the particle are updated due to the scattering event, if necessary.

8) If the current number of free flights is the same as the total number selected in step 1) then stop, otherwise using the updated momentum and energy of the particle return to step 2).

6.2 Ensemble Monte Carlo

The single particle Monte Carlo (MC) method produces a distribution function that omits cc-scattering. Therefore, its usefulness in situations where carrier-carrier interactions are important is limited. In the past, researchers have tried to include carrier-carrier interactions in a single particle MC calculation with an approximate form for the carrier-carrier scattering rate.

This still has the problem that the resulting distribution function is a one electron approximation. For this reason, an Ensemble Monte Carlo (EMC) formalism is preferred, especially when carrier-carrier scattering is important. In an EMC calculation, there are several interacting single particle MC calculations running simultaneously. This change increases the complexity and computational requirements needed for the simulation, but it also improves the accuracy of the calculation, particularly in the high energy region of the tail.

6.3 Our Ensemble Monte Carlo Calculations

Most of the calculations use a 21 by 21 by 21 k-space grid to compute the bandstructure of the materials. The computer code extrapolates the bandstructure between the k-space grid points. Several different types of bandstructures ranging from

single parabolic bands to local empirical pseudopotential bands [64] have been used. Initially the extrapolation between the grid points was done linearly, however the need to include cc-scattering with good energy conservation led us to implement a parabolic fitting.

Some calculations using a 41 k-point grid and linear fitting were done, but they are much more time consuming than 21 k-point calculations. The principal disadvantage of using a 21 k-point grid is that the low field results tend to be poor, especially in GaAs and InP. This occurs because in both materials the dominant phonon scattering mechanism at low fields is polar optical scattering in a shallow gamma valley.

The defect recombination rate coefficient r is treated as a constant for a given material. This produces an adjustable parameter that could be used to change the breakdown and lock-on fields. While changing r does not affect the qualitative behavior of the breakdown plots, it leads to results dependent on the assumptions about defect recombination.

To determine the initial carrier distribution in the EMC calculations, the computer code uses random numbers to place the carriers in k-space. In order to do this, a Maxwellian distribution of energies is assumed. Then the field accelerates the carriers in accord with Eq. 6.1. A random number is chosen for the first particle to determine if the carrier scatters either with other carriers or through phonon scattering. If none of the scattering events occurs, then the particle is virtually scattered. The code then determines if the second particle is scattered. Once all the particles are assessed, another time of free flight is randomly selected and the process begins again.

The code allows both optical and acoustic deformation potential scattering as well as polar optical scattering. The effects of piezoelectric scattering in GaAs, InP, and GaP are ignored because group III-V semiconductors are weakly piezoelectric [61]. Also in Si there is no polar optical or piezoelectric phonon scattering [61]. Derivations of the scattering rates for each phonon scattering mechanism can be found in Appendix A, and a more complete discussion is available in the work by Kang[11]. If an event is found, then the momentum and energy of the carrier or

carriers involved is updated.

The problem of how to include carrier-carrier scattering in the EMC calculations was resolved by assuming that neither the long-range nor the short-range events (in k-space) significantly alter the distribution function, which leaves only the mid range events to be calculated. The extremely short-range events occur often, but since the momentum exchanged is very small, their effect is minimal. Since such events are common, including them would require significantly increasing the number of flights. In contrast, the long range scattering events have larger momentum changes but the corresponding rates are so low that they almost never happen. This means that the events that are important fall into the intermediate region.

In order to simplify the calculations, the current computer code includes cc-scattering in only the first conduction band. This clearly produces errors. However, it is difficult to quantify these. For the fields of interest, the electrons are primarily within the first conduction band. Additionally the results suggest that the impact ionization and Auger rates are not strongly dependent on the electron distribution in the valence band.

The intermediate range events are treated by fitting a local parabola to the wavevector dependent bandstructure near the pair of carriers which may scatter and then calculating the scattering rate for the carriers as if they are on that parabola. The derivation of the rates is done Appendix B.

Once the EMC method has calculated the distribution function for a given field and carrier concentration, the code then calculates the impact ionization and Auger rates based on the calculated k-space distribution. To do this calculation, a table of all the possible impact ionization events is calculated separately beforehand based on the band structure. This calculation is discussed in the next section. Since Auger recombination is the inverse of impact ionization, an Auger table can be created simply from the impact ionization table. This approach makes the unstated assumption that the carrier distribution function is not significantly altered by the impact ionization process. While not true for high fields. This assumption may not be true for high

fields, but it s a reasonable approximation at low fields [65, 66]. This assumption has several advantages, not the least of which is that fewer flights are required to achieve steady state results.

6.4 Impact Ionization Table Calculation

The total impact ionization rate r_{ii} for a given carrier distribution function can be written as the sum of the impact ionization rates for each possible event in the grid. Mathematically, it takes the form

$$r_{ii} = \sum_{k_i} \sum_{k_{i'}} \sum_{k_f} \sum_{k_{f'}} S(k_i, k_{i'}, k_f, k_{f'}) f_{k_i} f_{k_{i'}} (1 - f_{k_f})(1 - f_{k_{f'}}) \tag{6.9}$$

where i and i' are the initial states, f and f' are the final states, and $S(k_i, k_{i'}, k_f, k_{f'})$ is the quantum mechanical scattering rate for each impact ionization event. The details for calculating the rates can be found in Appendix C.

Since calculating the value of $S(k_i, k_{i'}, k_f, k_{f'})$ does not depend on anything except the band structure, a separate code is used to create a table of possible impact ionization events and their corresponding $S(k_i, k_{i'}, k_f, k_{f'})$ values. Such a table would be far too large if it included every allowed set of $k_i, k_{i'}, k_f$, and $k_{f'}$ values, so instead the rates for a given k_i and $k_{i'}$ are first summed and then one set of k_f and $k_{f'}$ is chosen to represent the final states in the table.

Once the table is complete, it can be used to calculate both the impact ionization and Auger rates, since Auger recombination is the inverse of impact ionization. The Auger rates are calculated by simply interchanging the initial and final k point quantities.

In the literature [11, 65, 66, 67, 68], impact ionization has usually been described by the impact ionization coefficient, α. This quantity is related to the impact ionization rate coefficient, $C(F, n)$, defined in Eq. 5.1 as $\alpha = C(F, n)/v_d$, where v_d is the carrier drift velocity. For this comparison, v_d was set to its saturation value, 1×10^7 cm/s. In comparing the results for α in GaAs and Si and to those calculated by

others, reveals that the values in the literature are lower than those obtained here. This appears to be a consequence of the coarseness of the energy grid. For example, a carrier may need an energy of 3.2 eV to impact ionize, and such an energy can be within a cube which has a minimum energy of 2.4 eV. So if an electron with energy 2.5 is in the cube, because the table includes the total rate for all possible energies within the cube, the event is included. For this reason, a weighting factor is applied to the k-space distribution function of the carrier that initiated the impact ionization.

To calculate this weighting factor, a Maxwellian distribution is fitted to the minimum and maximum energies in the cube. Using the resulting effective temperature, the fraction of the total distribution with energies at or above E_i is calculated. This fraction is the weighting factor. The inclusion of the weighting factor does not effect the qualitative behavior of the rates, though it can alter them quantitatively.

To demonstrate the use of the weighting factor, a plot of the impact ionization coefficient α for GaAs is shown in Fig. 6.1. A linear extrapolation method is used for this comparison, since that is what other workers in this area apparently used [68, 67]. It is worth noting that switching to the quadratic extrapolation method also increases the impact ionization coefficient. This plot shows the results using the linear extrapolation both with (triangles) and without (circles and dotted line) weighting assuming a saturation drift velocity of $1 \times 10^7\ cm/s$ for all fields. The results of Jung [67] (solid curve) are plotted for comparison. I have also included the quadratic extrapolation impact ionization coefficient value (diamonds and dashed line), again assuming $v_d = 1 \times 10^7\ cm/s$.

6.5 Maxwellian Calculations

At high carrier densities, carrier-carrier (cc) scattering completely dominates the scattering events and such a situation results in a drifted Maxwellian distribution for the electrons at high densities [56]. This fact leads to a simple calculation of a distribution function at high density by approximating the drifted Maxwellian as a Maxwellian distribution.

The procedure is as follows. First, a Maxwellian distribution function at a given temperature and carrier concentration is assumed. Then a large number of carriers (10000) are placed randomly within the k-space volume based on the assumed distribution. Using this distribution and a table of possible events equivalent to the one used for the EMC calculation, the impact ionization and Auger rates are calculated. The rate of change of carrier density is then determined. This process is iterated to find the temperature for which the rate of change of carrier density becomes zero. This procedure defines the effective carrier temperature (T_c).

The resultant distribution is a Maxwelliancharacterized by an effective carrier temperature, T_c, that is much greater than the lattice temperature. To find the corresponding electric field the following calculations are done. A quasi-equilibrium

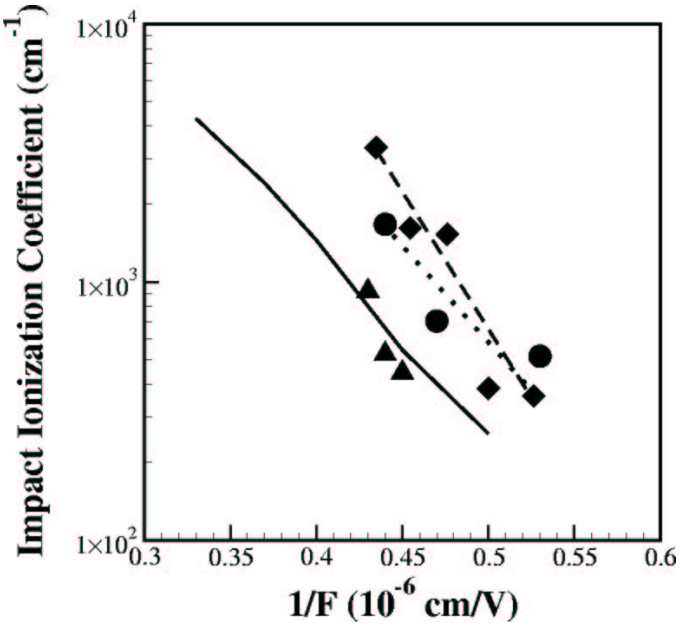

Figure 6.1: The impact ionization coefficient α as a function of inverse field for GaAs. The triangles are the results with the weighting factor. The circles and dotted line are the results without the weighting factor. The diamonds and dashed line are the results with the quadratic extrapolation. All of these results assume $v_d = 1 \times 10^7$ cm/s. The solid curve represents the results of Jung [67].

approximation is assumed, where the Joule heating is balanced by the phonon cooling. Therefore, the energy balance equation is

$$|qv_dF| = B(T_c), \tag{6.10}$$

where T_c is the carrier temperature, v_d is the drift velocity, F is the electric field, q is the charge, and $B(T_c)$ is the phonon-carrier cooling rate.

The phonon-carrier cooling rate can be expressed formally as

$$B(T_c) = \sum_{\vec{k}} \epsilon_{\vec{k}}[\lambda_-(\vec{k}) - \lambda_+(\vec{k})]f(\vec{k}, T_c) \tag{6.11}$$

where the sum is over the entire Brillouin zone, $\epsilon_{\vec{k}}$ is the phonon energy, and $f(\vec{k}, T_c)$ is the carrier distribution function. Consistent with the quasi-equilibrium approximation, this is assumed to be a Maxwell-Boltzmann distribution. $\lambda_-(\vec{k})$ and $\lambda_+(\vec{k})$ are the quantum mechanical phonon scattering rates for emission and absorption, respectively. From Fermi's Golden Rule, they have the form

$$\lambda_\pm(\vec{k}) = \frac{2\pi}{\hbar} \sum_{\vec{k'}} | < \vec{k}|H_{int}|\vec{k'} > |^2(1 - f_{\vec{k'}})\delta(E_{\vec{k}} - E_{\vec{k'}} \pm \epsilon_{|\vec{k'}-\vec{k}|}), \tag{6.12}$$

where $f_{\vec{k'}}$ is the occupation factor of state $\vec{k'}$ and $E_{\vec{k}}$ and $E_{\vec{k'}}$ are the band energies of the carrier with wavevectors $\vec{k}$ and $\vec{k'}$. In Eq. 6.12, $< \vec{k}|H_{int}|\vec{k'} >$ is the electron-phonon interaction Hamiltonian. This can be expressed in terms of the phonon scattering rates discussed in Appendix A.

Knowing the phonon cooling rate at T_c using Eq. 6.10, it is possible to calculate the field which corresponds to that temperature if the drift velocity is known. To further simplify this calculation, it is assumed that the inclusion of cc-scattering will not significantly effect the drift velocity. Still, the drift velocity is dependent on field, so an approximate drift velocity is first used and the resulting field is used in the computer code to calculate the drift velocity. Finally, using that velocity, the field corresponding to the temperature T_c is calculated.

There are three more important assumptions in this method. First, a Maxwellian distribution was assumed when technically it should be a drifted Maxwellian. Second, since the vast majority of the carriers are in the first conduction band for the fields of interest, the Maxwellian calculation uses the cooling rate for electrons in the first conduction band only. Third, the electrons and holes are assumed to have the same carrier temperature. Since the valence band distribution function is based on this temperature, this is a potential source of errors. However, this approximation should be acceptable because the results suggest that the impact ionization and Auger rates do not strongly depend on the valence band carrier distribution function.

CHAPTER VII
RESULTS

7.1 Breakdown Plots

The major results of this research can be summarized in breakdown plots. These plots are analogous to the schematic plots shown in Figs. 5.3 and 5.3. A breakdown plot show the density and field pairs which are in steady state, that is the rate of change of carrier density, defined in Eq. 5.1, is zero. These plots contain the results calculated using the EMC without cc-scattering, the EMC with cc-scattering, and Maxwellian methods. Since understanding these plots is key to understanding the results of this research, it is useful to discuss their general interpretation before discussing the results for a specific bandstructure. This is possible because each of the breakdown plots is qualitatively similar.

Figure 7.1 shows a breakdown plot for Model Material I. To make the low density results easier to observe, a close up of the low density region for Model Material one is shown in Fig. 7.2. (Model Material I will be discussed in greater detail in the next section.) The data points represent the densities that produce a steady state for a given field. The hollow circles represent the calculated curve obtained with the EMC method which does not include cc-scattering. This result can be viewed as somewhat unphysical since there is always carrier-carrier (cc) scattering. The EMC without cc-scattering can be viewed as the low density limit of the curve with cc-scattering, because when the density is low there is very little cc-scattering. The dashed curve, which represents the results without cc-scattering, is a fit based on the EMC results without cc-scattering. This fit is explained in the next section. The squares are the results for the Maxwellian calculations, which represent the high density limit. The solid circles are the EMC results, which include carrier-carrier scattering. The results including cc-scattering, which includes the EMC and high density Maxwellian calculations, were more difficult to fit to an analytic form. For this reason, the solid curve, which represents the results including cc-scattering, is primarily to guide the

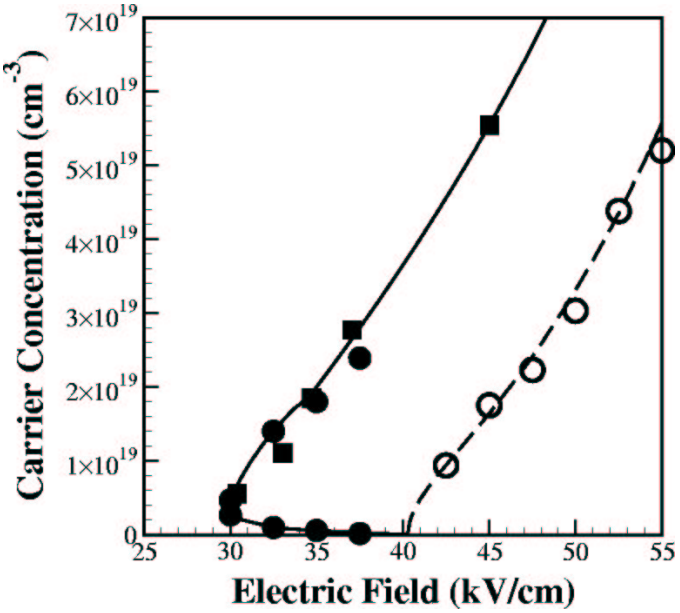

Figure 7.1: Breakdown plot for Model Material I ($E_g = 1.50eV$).

eye. The solid curve divides the plot into two regions, the region below the curve where rate of change of carrier density, defined by Eq. 5.1, is positive and the region below the curve where rate of change of carrier density is negative. Thus all combinations of

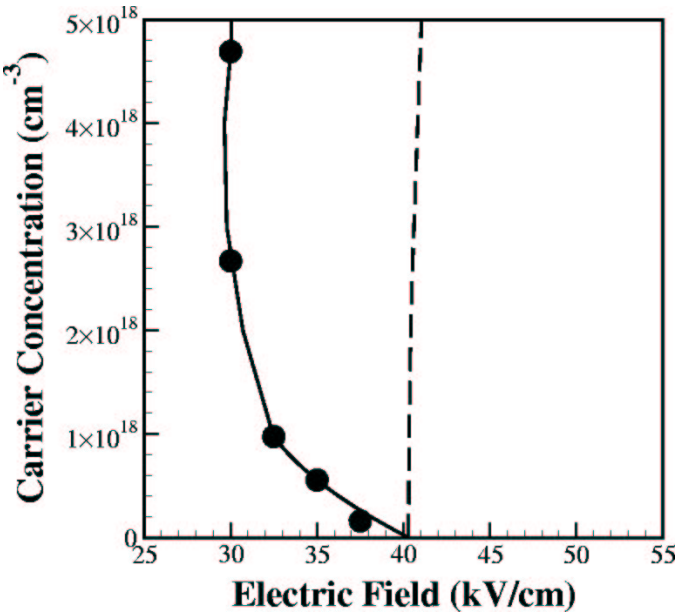

Figure 7.2: A blow up of the low carrier conecentration range in Fig. 7.1.

field and carrier density which lie below the solid curve will produce a net increase of carrier density until a steady state is reached. Similarly, all combinations above the curve will experience a net decrease in carrier density until steady state is reached. The EMC results including cc-scattering are the most accurate. However in practice, obtaining them requires substantially more computational time than either of the other methods used. The inclusion of carrier-carrier (cc) scattering becomes more complicated for realistic bandstructures, and thus the model material calculations are useful guides for the calculations with realistic bandstructures.

As mentioned in section 5.3, in order to simplify the discussion of the breakdown plots, it is assumed that rising carrier density will not effect the field across the switch.

Using Fig. 7.1, Fig. 7.2, and Eq. 5.1 as an example, each plot can be interpreted as follows. If the field is less than 30 kV/cm, then regardless of the carrier density (and whether or not carrier-carrier scattering is included in the calculations), the only steady state solution is $n = 0$. Therefore, any non-zero carrier density n will decrease to zero. The lowest field for which there is a non-zero steady state carrier density is 30 kV/cm. This minimum field is the predicted lock-on field, F_{LO}. If the field is 32.5 kV/cm, then there are three different carrier density ranges. If the carrier density is below 9.4×10^{17} cm^{-3}, then there will be a decrease in carrier density until the carrier density reaches the $n = 0$ steady state. If the carrier density is greater than 9.4×10^{17} cm^{-3} but less than 1.4×10^{19} cm^{-3}, then it will increase until it reaches the steady state value, given by the solid curve, of 1.4×10^{19} cm^{-3}. If the carrier density is greater than 1.4×10^{19} cm^{-3} then the carrier density will drop down to 1.4×10^{19} cm^{-3}. This means the maximum steady state carrier density is a stable steady state while the lower steady state carrier density is unstable. The lower unstable steady state carrier density can be thought of as the injected carrier density necessary to initiate low field steady state breakdown.The existence of a maximum carrier density is one of premises of this approach to breakdown. Of course, that maximum may be so large that the material would physically be damaged before n reaches that maximum. Another point worth noting is the field for which the EMC

results without carrier-carrier scattering first have a non-zero steady state solution. In this case 40.3 kV/cm. This is the intrinsic breakdown field F_B. Once this field is reached, a very small number of carriers will begin producing more and more carriers.

Breakdown theories suggest that the number of carriers at breakdown will increase to infinity because no steady state is possible above the breakdown field [49, 50, 51, 52, 53]. However, this theory predicts that at breakdown the carrier density will be large but finite. One reason is the inclusion of Auger recombination. For example, an examination of Fig. 7.1 shows that when the intrinsic breakdown field is reached, the carrier density will begin to increase until it reaches approximately 4×10^{19} cm^{-3}.

7.2 Results For Model Material I ($E_g = 1.50eV$)

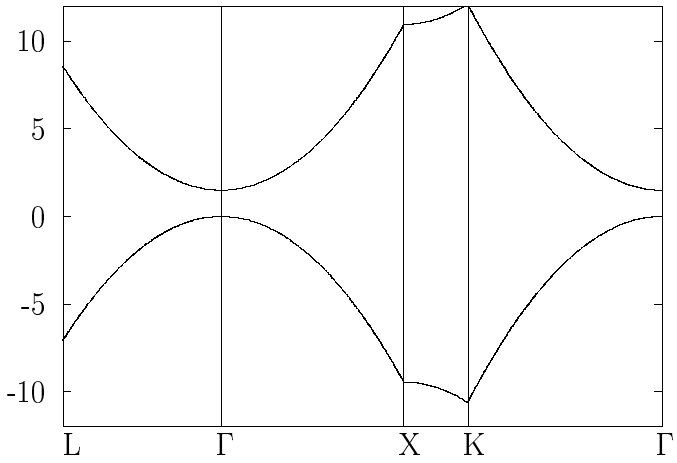

Figure 7.3: The bandstructure plot for Model Material I.

In order to test the conceptual validity of this approach, it is first applied to a model material with a simple parabolic bandstructure. This bandstructure has single valence and single conduction bands, that both with effective masses of 0.5 m_e. Because this method will be applied to lock-on in GaAs and InP, a band gap close to that of the real materials in question, 1.5 eV, was chosen. A plot of the simple bandstructure for this material, that is labelled Model Material I, is shown in Fig. 7.3.

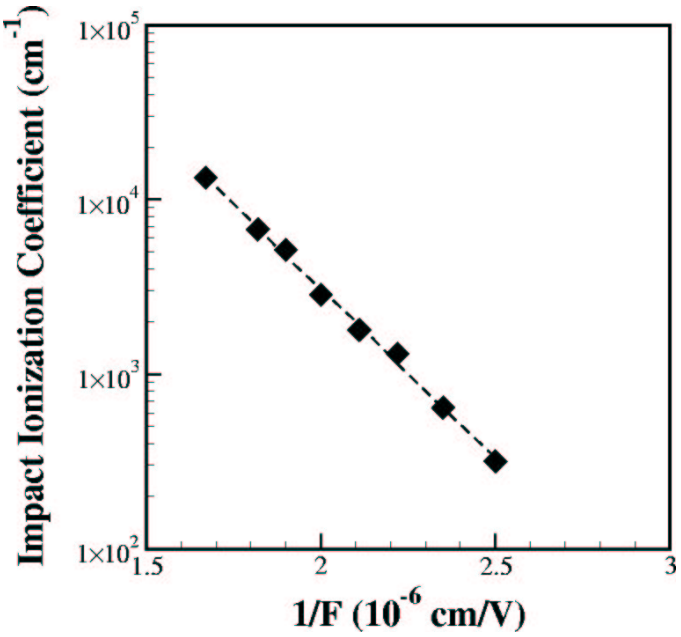

Figure 7.4: The impact ionization coefficient α as a function of inverse field for Model Material I.

In order to simplify the calculations, the only type of phonon scattering included in these model material calculations is acoustic deformation potential scattering. This type pf phonon scattering was chosen because it produces a non-Maxwellian distribution function except in the case of very low fields [56]. The acoustic deformation potential and several other parameters are listed in Table 7.1.

If there is no cc-scattering it is possible to fit both the impact ionization rate

Number of particles in cond. and val. band	100
Lattice constant, a_{lat}	5.64
Mass density, ρ	5.31 g/cm^3
Speed of sound, v_s	5.2×10^5 cm/s
Acoustic deformation potential, D_a	10 eV
ϵ_0	12.9

Table 7.1: Simulation parameters for for Model Material I.

and Auger rate to functions of the electric field F. Doing these fits produces an approximate closed form for $R(F, n)$, defined in Eq. 5.2, given an assumed defect recombination rate r. For the model materials, the assumption $r = 1 \times 10^9 s^{-1}$ is used. It is common to use the impact ionization coefficient, α, as a function of inverse field to show the field dependence of impact ionization [11, 65, 66, 67, 68]. In terms of the quantities used in Eq. 5.3, $\alpha = C(F)/v_d$ where v_d is the drift velocity. To calculate α for the model material, and the materials which follow, the drift velocity was calculated for each field without including the effects of cc-scattering. Figure 7.4 shows the EMC results without cc-scattering for α for this model material. From that figure it can be readily seen that α depends exponentially on $1/F$. A similar plot can clearly be made for the function $C(F)$. The computed $C(F)$ can thus be easily fit to the exponential dependence assumed in Section 5.1. The theoretical Auger rate coefficient, a can be readily fit to a linear function of field. Thus, it has the form $a = a_0 + a_1 F$ where a_1 is negative. A plot of the Auger rate coefficient for Model Material I is shown in Fig. 7.5.

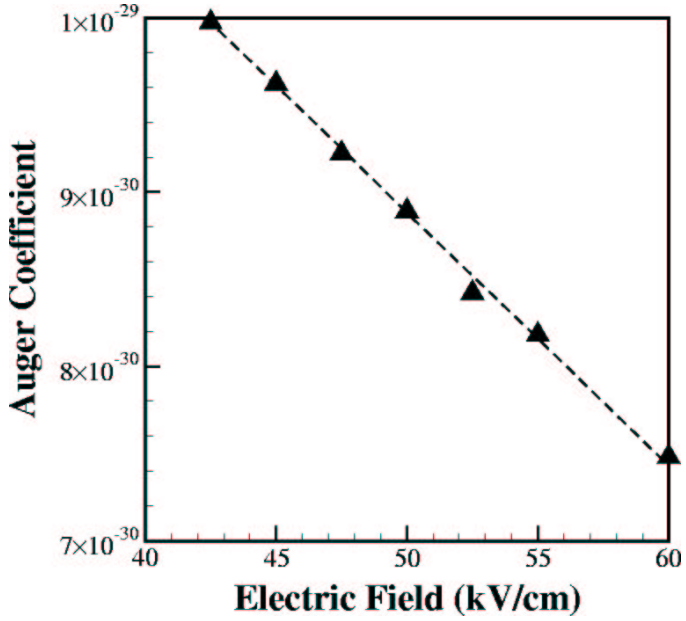

Figure 7.5: The Auger rate coefficient, a, as a function of field for Model Material I.

Inserting these fitting functions into Eq. 5.3, produces the following approximation

for $R(F,n)$:

$$R(F,n) = \alpha_0 e^{-\beta/F} - (a_0 + a_1 F)n^2 - r = 0. \tag{7.1}$$

This expression can be solved numerically to find the values of n and F for which $R = 0$. This can be done for all the materials discussed in this dissertation. In other words, the form in Eq. 7.1 is used to calculate the dashed curves in Fig. 7.1 all other breakdown plots in this chapter.

Unfortunately the EMC results with cc-scattering are not so easily fit to assumed analytic forms. For this reason, the solid curves on the breakdown plots have been inserted through the EMC and high density Maxwellian results to help to guide the eye.

One of the guiding assumptions is that cc-scattering should turn a non-Maxwellian carrier distribution function into a Maxwellian distribution at high carrier densities.

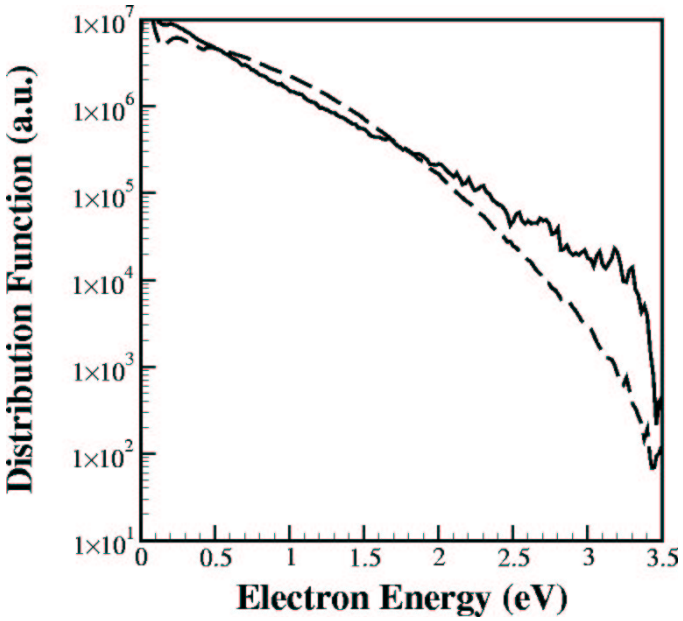

Figure 7.6: The distribution function as a function of electron energy for Model Material I when $F = 37.5\ kV/cm$ and $n = 5.54 \times 10^{19}\ cm^{-3}$ with (solid curve) and without (dashed curve) cc-scattering.

This means that, at high density, the distribution function from an EMC calculation including cc-scattering should approach a Maxwellian distribution. In contrast, the distribution function from a similar calculation which does not include cc-scattering should be noticeably different from the EMC result which includes cc-scattering. Figure 7.6 shows the calculated distribution function both with (solid curve) and without (dashed curve) cc-scattering for Model Material I at $F = 37.5\ kV/cm$ and $n = 5.54 \times 10^{19}\ cm^{-3}$. Clearly, the solid curve is approaching a Maxwellian form. This result confirms the guiding assumption of collective impact ionization theory just discussed.

Since increasing the carrier density alters the distribution function, the impact ionization rate coefficient should also depend on carrier density. This can be seen in Fig. 7.7. This log-log plot shows the calculated impact ionization rate for Model Material I as a function of carrier density for $F = 37.5\ kV/cm$ with (solid triangles) and without (stars) cc-scattering. On a log-log plot, the slope corresponds to the

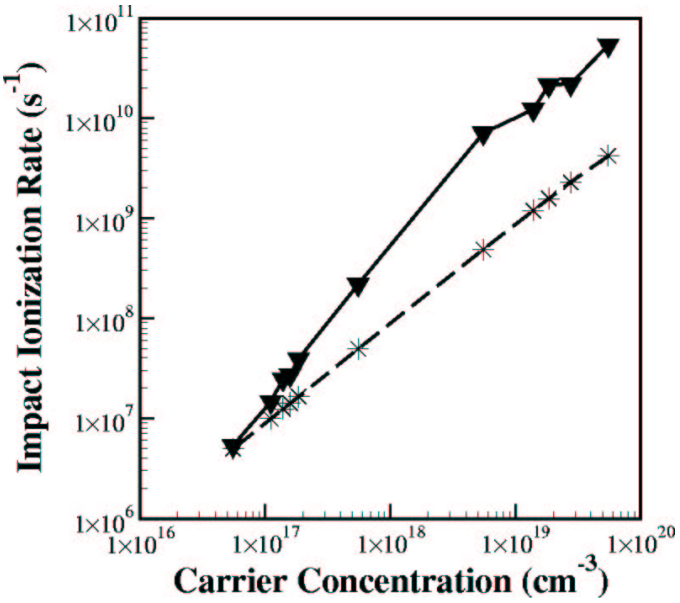

Figure 7.7: The impact ionization rate as a function of carrier density when $F = 37.5$ kV/cm for Model Material I with (solid triangles, solid lines) and without (stars, dashed lines) cc-scattering.

power dependence of the rates. The rates without cc-scattering show the expected nearly linear dependence on n. The rates with cc-scattering show a dependence closer to $n^{1.6}$. Examining the high density curve that includes cc-scattering, the slope is approaching the slope of the curve without cc-scattering. This suggests a type of density saturation effect. That is, there is s density above which cc-scattering causes little or no further enhancement of the impact ionization rate. This makes conceptual sense because, once a carrier distribution function is Maxwellian, it cannot become "more" Maxwellian.

Because the inclusion of cc-scattering alters the carrier distribution function, the Auger rate, like the impact ionization rate, should be affected by the inclusion of cc-scattering. Thus the Auger rate coefficient should be carrier density dependent. The results show that there is a small effect on the Auger rate coefficient when cc-scattering is included. This effect tends to decrease the Auger rate coefficient slightly rather than increase it. This effect is often so small that it is difficult to separate from random fluctuations, but it does seem to be present.

The breakdown plot results for this Model Material I are shown in Fig. 7.1. As previously discussed, they can thus be summarized as follows. The predicted intrinsic breakdown field F_B is 40.3 kV/cm, and the predicted lock-on field F_{LO} is 30 kV/cm. Though the intrinsic breakdown field is far lower than for most real materials, these results do show the behavior predicted by the schematic analysis done in Sections 5.1 and 5.2.

The breakdown plot in Fig. 7.1 can now be readily compared to Figs. 5.1 and 5.4. The results for Model Material I clearly reproduce the expected S-like behavior that was assumed in the development of collective impact ionization theory.

7.3 Results For Model Material II ($E_g = 0.75eV$)

One of the obvious differences between Si, GaAs, and InP is the band gap. For this reason, the model material calculations are repeated for a model material with a bandgap of 0.75 eV, but which is otherwise identical to Model Material I. This material

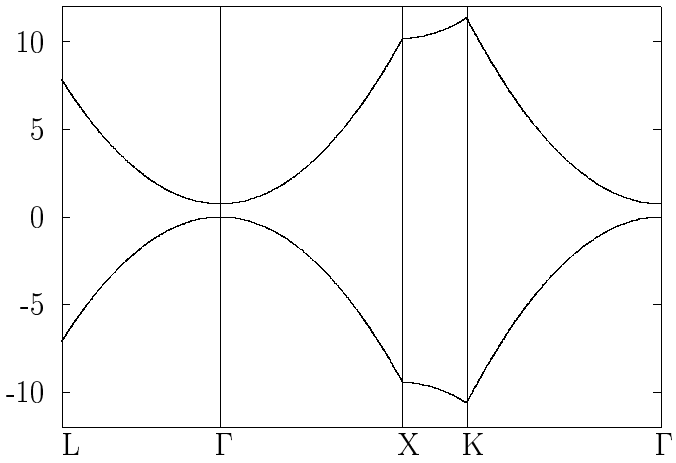

Figure 7.8: The Model Material II bandstructure plot.

is referred to as Model Material II. Comparison of these results helps determine the effect that changes in the band gap will have on the lock-on and breakdown fields. Figure 7.8 shows the bandstructure used in this case. All parameters used in the simulations (except the bandgap) were the same in Model Materials I and II. The

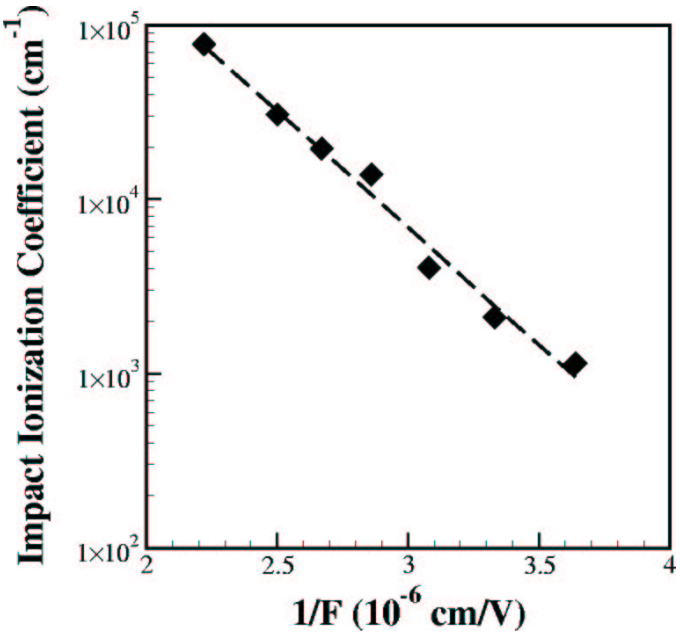

Figure 7.9: The impact ionization coefficient α as a function of inverse field for Model Material II.

simulation parameters which describe Model Material II can therefore be found in Table 7.1.

In Fig. 7.9, the impact ionization coefficient α is plotted for Model Material II. An examination of Figs. 7.9 and 7.4 allows a comparison of the impact ionization coefficients for the two model materials and their dependence on F. Similar to the the impact ionization coefficient for Model Material I, α for Model Material II has an exponential dependence on F^{-1}. Comparing the two impact ionization coefficients for a given field, shows that shrinking the band gap by a factor of two has increased the impact ionization coefficient by a factor of approximately 100.

The calculated Auger rate coefficient for Model Material II is plotted as a function of field Fig. 7.10. Comparing Figs 7.5 and 7.10 reveals that halving the bandgap caused an enhancement of the Auger rate coefficient. However, the Auger enhancement is only about a factor of three. The Auger rate coefficient for Model Material II depends linearly on F, and this allows the use of Eq. 7.1 to fit these results.

Figure 7.11 shows the breakdown plot for this model material. The predicted

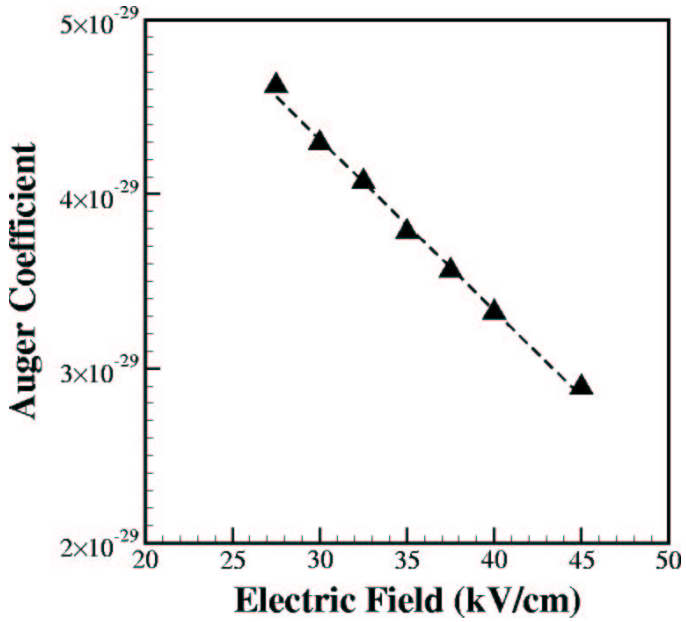

Figure 7.10: The Auger rate coefficient, a, as a function of field for Model Material II.

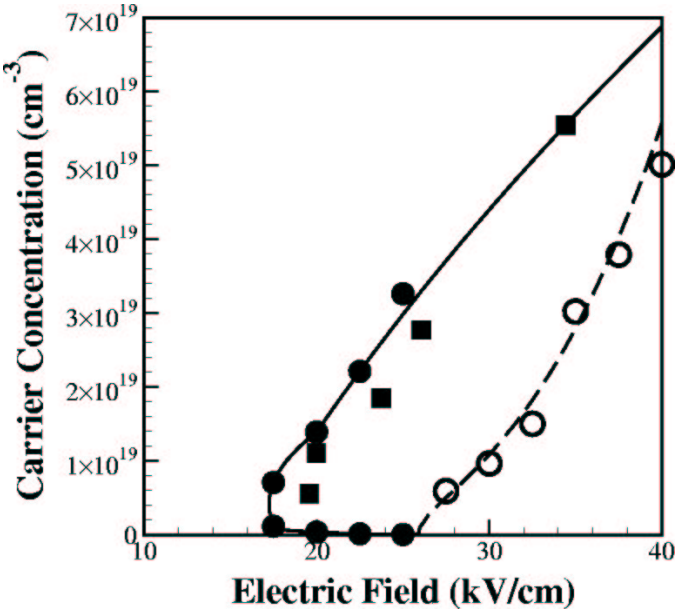

Figure 7.11: Breakdown plot for Model Material II.

intrinsic breakdown field F_B is 25.9 kV/cm and the predicted lock-on field F_{LO} is 17.5 kV/cm. As expected, shrinking the band gap resulted in a reduction of both the breakdown field and the lock-on field. However, shrinking the band gap does not affect the qualitative breakdown plot behavior.

7.4 Results For Gallium Arsenide (GaAs)

The bandstructure used in the simulations for GaAs is shown in Fig. 7.12. It contains two conduction bands and one valence band. It was calculated using the local empirical pseudopotential method [64], with Cohen and Bergstresser form factors [64]. The GaAs parameters used in the calculations are shown in Table 7.2.

The calculated impact ionization coefficient and the Auger rate coefficient for GaAs without cc-scattering are shown in Figs. 7.13 and 7.14, respectively. While there is some scatter to the GaAs results for the impact ionization coefficient, it is still possible to fit them to an exponential function of F^{-1}, as in Eq. 7.1. The Auger rate coefficients shown in Fig. 7.14 show the anticipated linear dependence on F. Because the characteristic recombination time in GaAs is approximately between 1

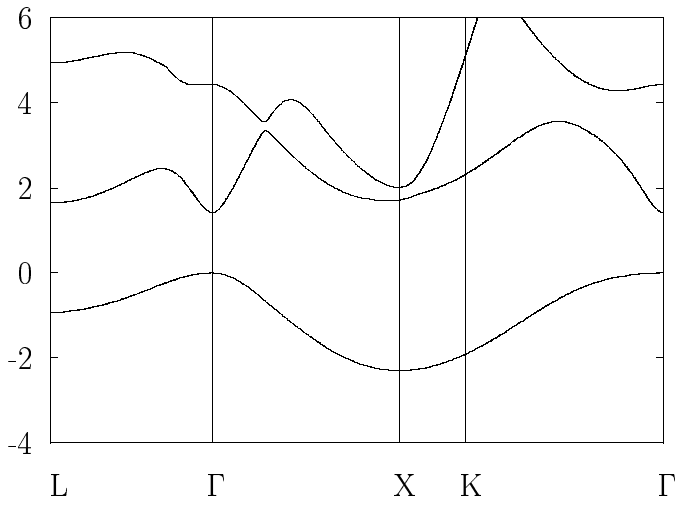

Figure 7.12: GaAs bandstructure plot.

and 10 nanoseconds [69], the defect recombination rate r, for the GaAs calculations, was set to $r = 1 \times 10^9 s^{-1}$.

The breakdown plot for GaAs is shown in Fig. 7.15. Based on Eq. 7.1, the breakdown results from the EMC calculations without cc-scattering predict an intrinsic breakdown field F_B for GaAs of 177 kV/cm. When working with PCSS's, the team

Number of particles in cond. and val. band	100
Lattice constant, a_{lat}	5.64
Mass density, ρ	5.37 g/cm^3
Speed of sound, v_s	5.22×10^5 cm/s
Acoustic deformation potential, D_a	5.0 eV
Optical deformation potential, D_0	2.1×10^8 eV/cm
Opt. def. phonon energy, $\hbar\omega_0$	0.03 eV
Polar optical phonon energy, $\hbar\omega_{po}$	0.036 eV
ϵ_0	13.18
ϵ_{inf}	10.89

Table 7.2: Simulation parameters for GaAs

at Sandia National Labs found that the GaAs switches would fail without any optical triggering (the onset of intrinsic breakdown) for fields as large as 143 kV/cm [4]. In order to get GaAs to fields this high, it was necessary to use water to reduce surface flashover. While the breakdown observed in GaAs PCSS's was often due to surface breakdown, this was the maximum in spite of numerous attempts to improve hold off voltage. Using this number also minimizes the effect of different physical geometries since the same type of switches were used both the observe lock-on and test for breakdown. Finally, this value is in reasonable agreement with the intrinsic breakdown fields for GaAs listed by others (100-250 kV/cm [69, 70] and 80-100 kV/cm [71]. The value of 143 kV/cm compares reasonably with the predicted intrinsic breakdown field of 177 kV/cm. It is probably possible to improve this matching by changing the defect recombination rate.

As can be seen in Fig. 7.15, several data points have been obtained using the EMC calculations including cc-scattering. The breakdown results from the Maxwellian approximation, shown in Fig. 7.15, predict a lock-on field F_{LO} for GaAs of approxi-

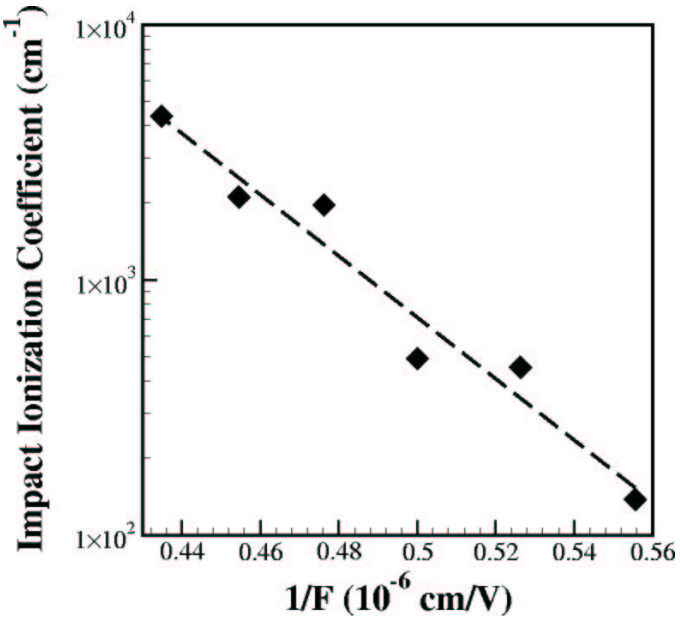

Figure 7.13: The impact ionization coefficient α as a function of inverse field for GaAs.

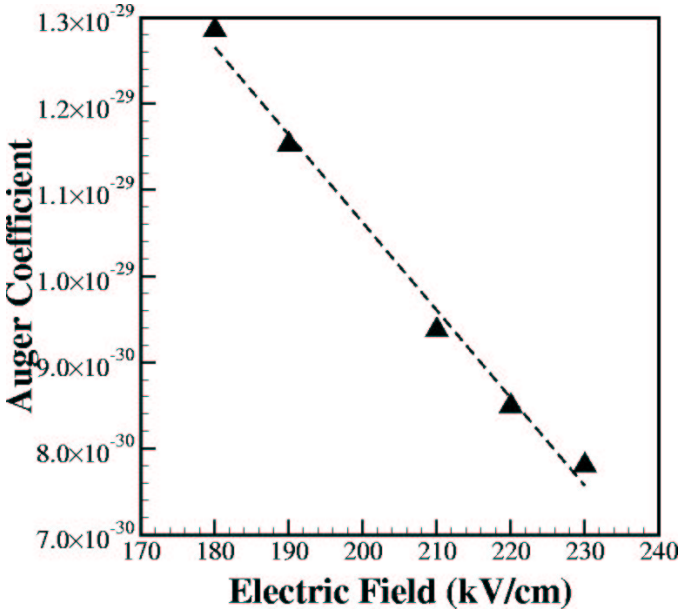

Figure 7.14: The Auger rate coefficient, a, as a function of field for GaAs.

mately 91 kV/cm. The experimental lock-on field in GaAs is approximately 3.5-9.5 kV/cm [8]. The predicted field is thus too high by a factor of between 10 and 20. The reasons for this experimental-theoretical disagreement are not known. However,

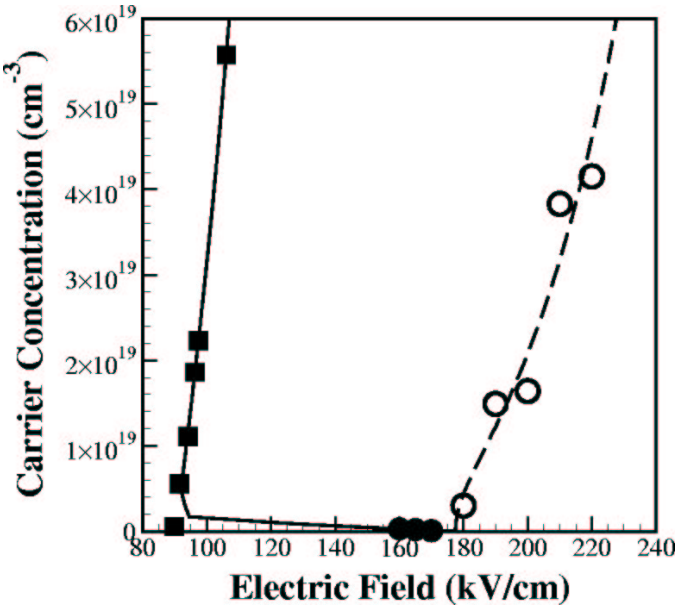

Figure 7.15: Breakdown plot for GaAs.

a lower lock-on field could result if the defect recombination rate were decreased.

Because collective impact ionization theory assumes that the carrier distribution will become Maxwellian at high fields and carrier densities, it is interesting to calculate the carrier distribution function in GaAs near the predicted intrinsic breakdown field of 177 kV/cm and to compare it with a Maxwellian distribution at a similar field. Such a comparison is made in Fig. 7.16. In that figure, the distribution function in GaAs calculated at $F = 180$ kV/cm using the EMC method without cc-scattering (solid curve) is compared with an approximate Maxwellian distribution (dashed curve) for this field. As previously discussed, the impact ionization rate depends approximately on the area under the curves for energies above the vertical dotted line, which is the calculated GaAs bandgap, $E_g = 1.415$ eV. As can be seen from the figure, the EMC distribution without cc-scattering is very non-Maxwellian. Therefore, the inclusion

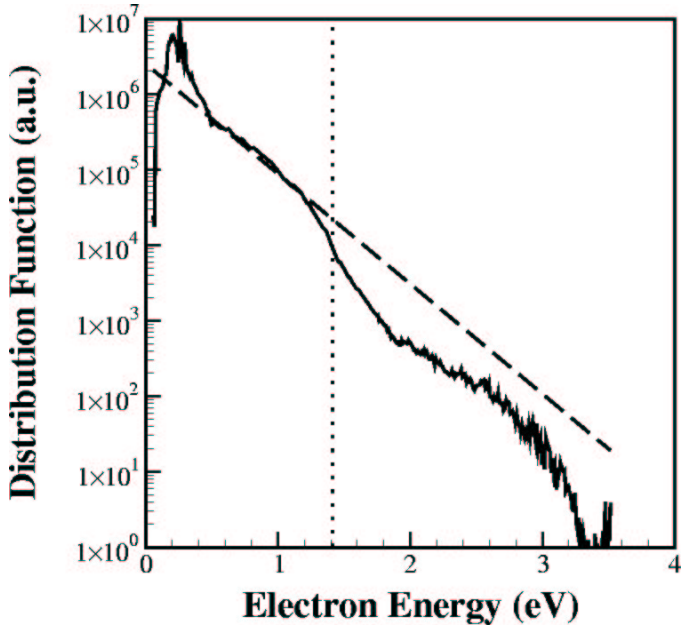

Figure 7.16: The distribution function as a function of carrier energy for GaAs when F=180 kV/cm. The solid curve is the EMC distribution function without cc-scattering, and the dashed curve is an approximate Maxwellian distribution. The dotted line marks the energy gap of 1.415 eV.

of cc-scattering in the EMC simulations is expected to produce major effects. This is confirmed by the fact that the predicted breakdown and lock-on fields are far apart.

7.5 Results For Indium Phosphide (InP)

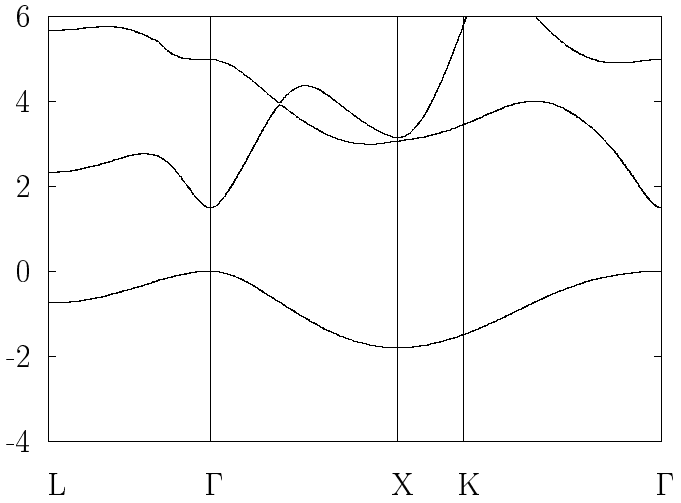

Figure 7.17: InP bandstructure plot.

The bandstructure used in the simulations for InP is shown in Fig. 7.17. It was calculated using the local empirical pseudopotential method [64], with Fischetti form factors [68]. For these calculations, only the first valence band and the first two conduction bands are used.

For InP polar optical, optical deformation potential, and acoustic deformation potential scattering are included. The parameters used to calculate these scattering mechanisms, as well as to calculate the impact ionization table, for InP are shown in Table 7.3.

The impact ionization coefficient for InP, computed without cc-scattering, is plotted as a function F^{-1} in Fig. 7.18. It has the expected exponential dependence on inverse field as assumed in Eq. 7.1. The Auger rate coefficients, plotted in Fig. 7.19, can be fit reasonably well to a linear function of F. This allows a fit to the data without cc-scattering using Eq. 7.1. In this instance, the value of r was chosen to give InP a breakdown field approximately the same as that of GaAs. Assuming the

Number of particles in cond. and val. band	100
Lattice constant, a_{lat}	5.86
Mass density, ρ	4.81 g/cm^3
Speed of sound, v_s	5.13×10^5 cm/s
Acoustic deformation potential, D_a	5.0 eV
Optical deformation potential, D_0	2.0×10^8 eV/cm
Opt. def. phonon energy, $\hbar\omega_0$	0.042 eV
Polar optical phonon energy, $\hbar\omega_{po}$	0.042 eV
ϵ_0	12.61
ϵ_{inf}	9.61

Table 7.3: Simulation parameters for InP

defect recombination rate $r = 1 \times 10^8 s^{-1}$, the predicted intrinsic breakdown field F_B for InP is 173 kV/cm. The experimentally observed breakdown field is 130 kV/cm for InP [71]. The experimental field is in reasonable agreement with the results.

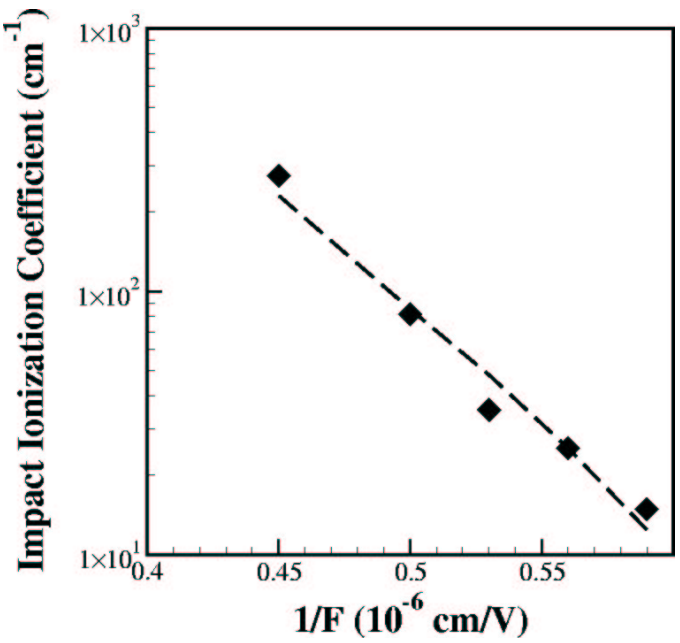

Figure 7.18: The impact ionization coefficient α as a function of inverse field for InP.

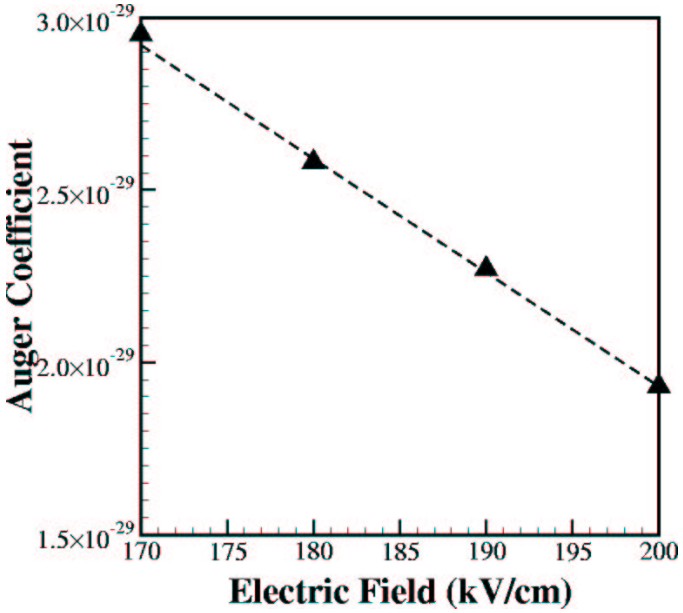

Figure 7.19: The Auger rate coefficient, a, as a function of field for InP.

Because the collective impact ionization theory assumes the carrier distribution will become Maxwellian at high enough fields and carrier densities, it is of interest to calculate the carrier distribution function in InP near the predicted intrinsic breakdown field of 173 kV/cm and to compare it with a Maxwellian distribution at a similar field. Such a comparison is made in Fig. 7.20. In that figure, the distribution function in InP that is calculated at $F = 180$ kV/cm using the EMC method without cc-scattering (solid curve) is compared with an approximate Maxwellian distribution (dashed curve) for this field. This figure is similar to Fig. 5.2. The impact ionization rate will depend approximately on the area under the curve for energies above the vertical dotted line, which corresponds to the InP bandgap energy, $E_g = 1.494$ eV. As can be readily seen, the EMC distribution without cc-scattering is noticeably non-Maxwellian and the inclusion of cc-scattering is therefore expected to produce major effects.

Several data points were obtained including the effects of cc-scattering; they are shown in Fig. 7.21. The breakdown results from the Maxwellian approximation, shown in Fig. 7.21, predict a lock-on field F_{LO} for InP of 40 kV/cm.

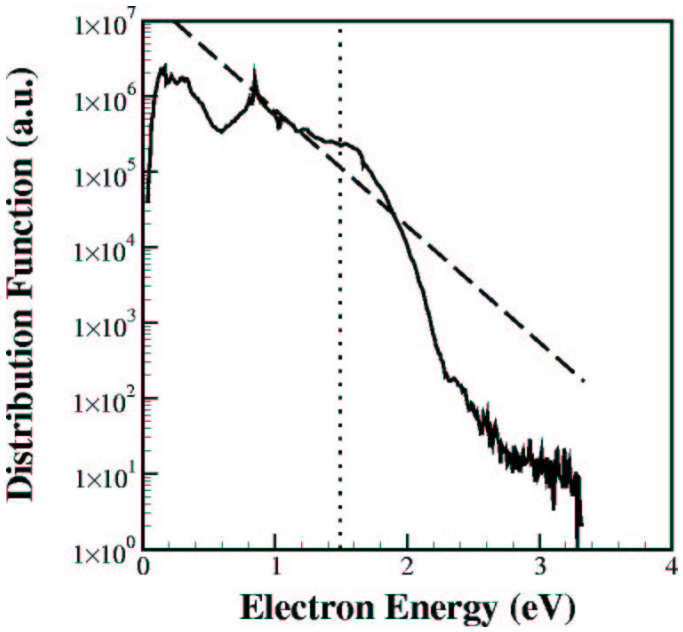

Figure 7.20: The distribution function as a function of carrier energy for InP when F=180 kV/cm. The solid curve is the EMC distribution function without cc-scattering, and the dashed curve is an approximate Maxwellian distribution. The dotted line marks the energy gap of 1.494 eV.

The experimental lock-on field in InP is around 14.4 kV/cm [24]. In comparison with experiment, the calculated lock-on field is thus in error by a factor of 3. The reasons for this experimental-theoretical disagreement are not known. However, it is worth noting again that the predicted F_{LO} could be changed by changing the defect recombination rate r.

While GaAs and InP have similar breakdown fields, the InP predicted lock-on field is much lower than GaAs lock-on field. One reason for this difference can be seen by comparing Figs. 7.16 and 7.20. Both compare the distribution functions with approximate Maxwellian distribution functions. Based on these plots, GaAs will show significant enhancement in its impact ionization rate if the distribution function becomes Maxwellian. However, InP will clearly show a greater enhancement of this rate which will lead to a larger difference between the lock-on and breakdown

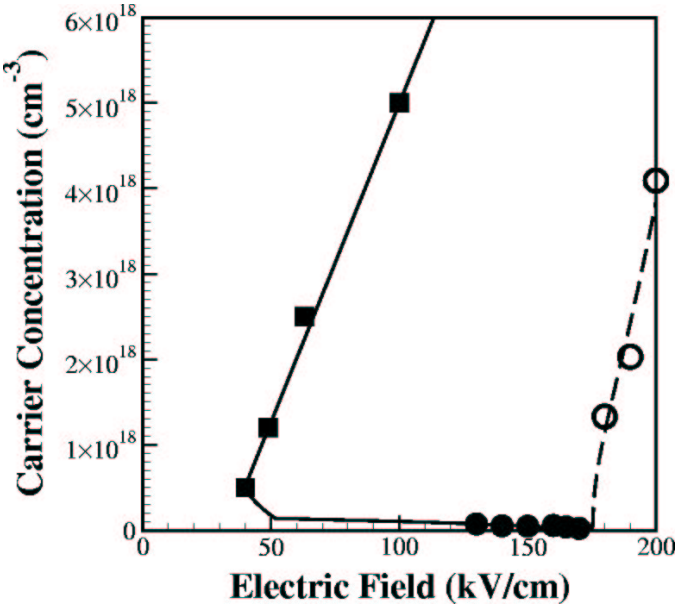

Figure 7.21: Breakdown plot for InP.

fields.

7.6 Results For Silicon (Si)

The Si bandstructure used in the calculations is shown in Fig. 7.21. This was calculated using the local empirical pseudopotential method of Cohen and Bergstresser

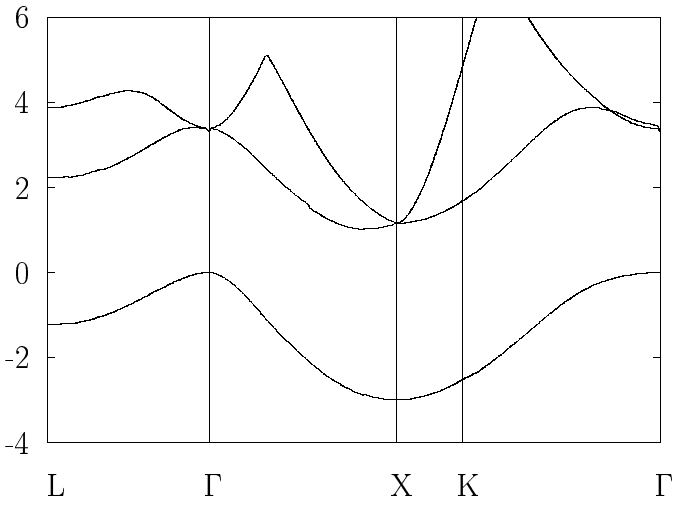

Figure 7.22: Silicon bandstructure plot.

[64] along with Kunikiyo's improved form factors [65]. As noted in Section 6.3, the simulations for Si include only optical and acoustic deformation potential phonon scattering. Further, following the method of Fischetti [68], there are different acoustic and optical deformation potentials in each band. Since Kunikiyo's bands are used and Fischetti's method of treating the phonon scattering, the deformation potentials are different then those of Fischetti [68]. A complete list of the parameters used in these simulations is given in Table 7.4.

The EMC calculations for Si without cc-scattering provided results similar to those for the other materials. The impact ionization coefficient has the expected field dependence, as is shown in Fig. 7.23. However, there is disagreement with the expected linear field dependence for the Auger rate coefficient as can be seen in Fig. 7.24. However, this discrepancy looks worse than it is, because the percentage difference between the highest and lowest values is only 6%.

For the breakdown plot for Si, a defect recombination rate of $r = 1 \times 10^9 s^{-1}$ is

Number of particles in cond. and val. band	100
Lattice constant, a_{lat}	5.43
Mass density, ρ	2.33 g/cm^3
Speed of sound, v_s	9.18×10^5 cm/s
Acoustic deformation potential for val. band	6.5 eV
Acoustic deformation potential for 1st cond. band	2.4 eV
Acoustic deformation potential for 2nd cond. band	3.4 eV
Optical deformation potential for val. band	5.0×10^8 eV/cm
Optical deformation potential for 1st cond. band	1.75×10^8 eV/cm
Optical deformation potential for 2nd cond. band	2.1×10^8 eV/cm
Opt. def. phonon energy, $\hbar\omega_0$	0.062 eV
ϵ_0	11.7

Table 7.4: Simulation parameters for Si

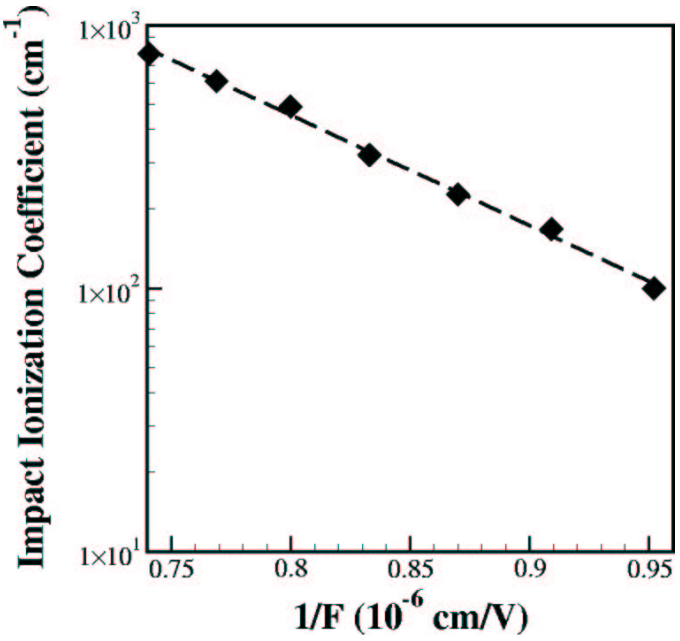

Figure 7.23: The impact ionization coefficient α as a function of inverse field for Si.

used. The breakdown plot results obtained using the EMC without cc-scattering, the EMC including cc-scattering, and the Maxwellian methods are shown in Fig. 7.25.

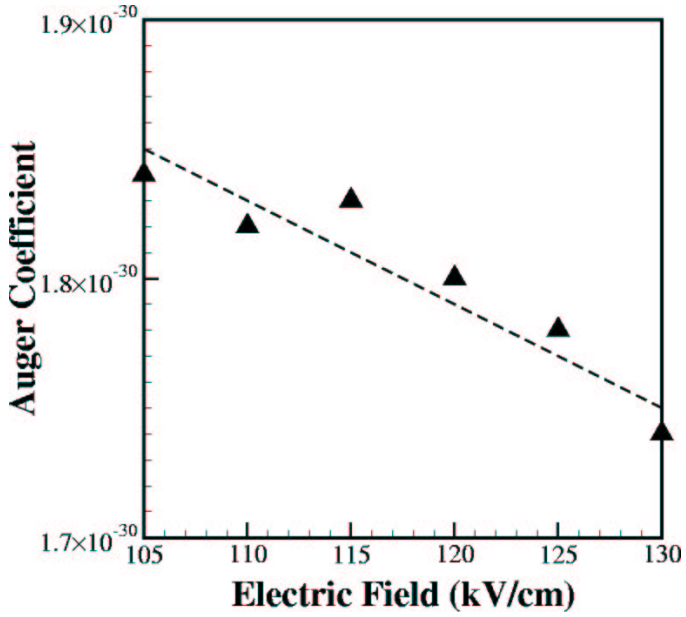

Figure 7.24: The Auger rate coefficient, a, as a function of field for Si.

As can be seen from that figure, the predicted intrinsic breakdown field for Si is approximately $F_B = 104\ kV/cm$. Experimental work done at Sandia shows that a Si PCSS has a maximum breakdown field of 91 kV/cm [4, 8]. Similar to the GaAs experimental results discussed above, the Si PCSS's are prone to surface flashover which is mitigated by using water to reduce surface flashover. This value compares well with the predicted intrinsic breakdown field of 104 kV/cm.

The EMC results including cc-scattering can be used to predict a lock-on field for Si. From these results, shown in Fig. 7.25, a predicted lock-on field of $F_{LO} = 77\ kV/cm$ is obtained. It is worth noting here that the results from the Maxwellian approximation, shown in the same figure, predict a slightly higher Si lock-on field of 90 kV/cm.

These results show that there is a smaller difference between the predicted lock-on and breakdown fields for Si than there is for GaAs and InP. A reason for this can be understood by looking at the carrier distribution function at a field near the predicted breakdown field. Figure 7.26 shows Si distribution functions at the field $F = 105\ kV/cm$ computed using the EMC (without cc-scattering) and the Maxwellian

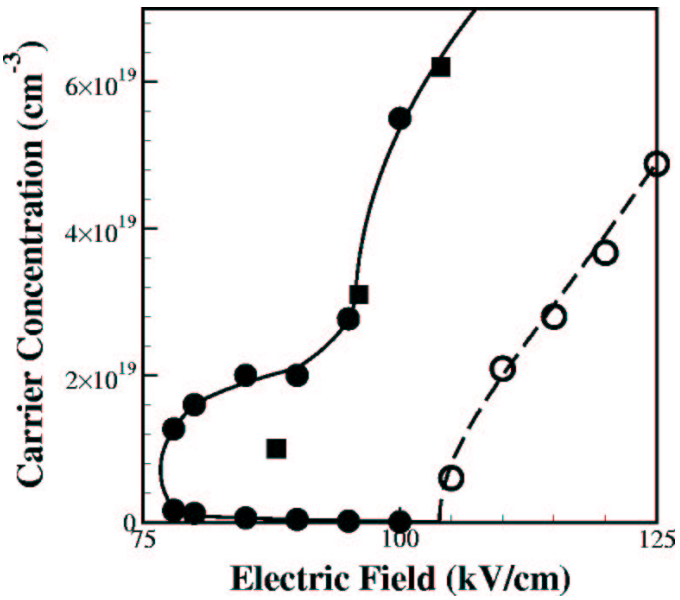

Figure 7.25: Breakdown plot for Si.

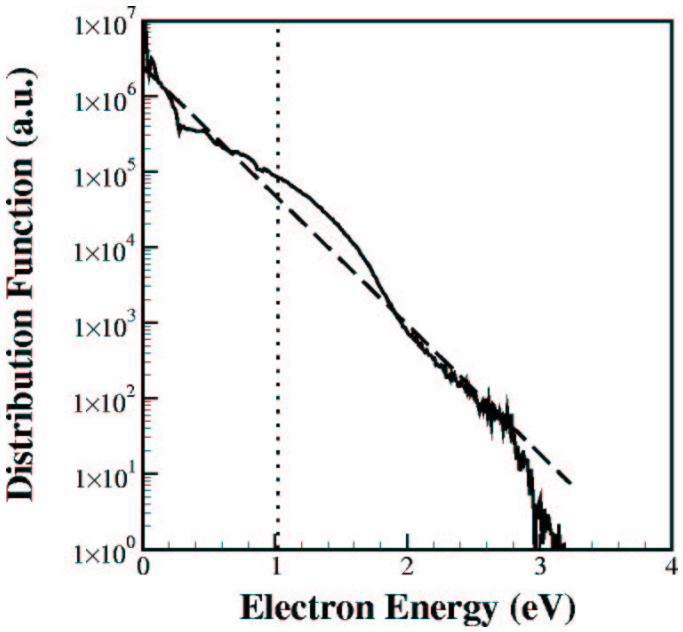

Figure 7.26: The distribution function as a function of carrier energy for Si when $F = 105\ kV/cm$. The solid curve is the EMC distribution function without cc-scattering, and the dashed curve is an approximate Maxwellian distribution. The dotted line marks the energy gap of 1.024 eV.

methods. From that figure, there are clearly only small differences between the two distributions, especially at energies larger than one bangap ($E_g = 1.024$ eV, shown as the vertical dotted line in Fig. 7.26) above the conduction band edge. This shows that, at energies above the impact ionization threshold, the high field distribution in Si is close to a Maxwellian, even without including cc-scattering. Thus, including cc-scattering in the EMC simulations is not expected to change the distribution very much. It is also therefore not expected to lead to as great an enhancement of the impact ionization rate as it does for GaAs and InP for which the the EMC distribution without cc-scattering and the Maxwellian show much greater differences.

The EMC including cc-scattering results predict a difference between the break-down field and the lock-on field in Si of about $F_B - F_{LO} \approx 27\ kV/cm$. For both GaAs and InP, the results predict that this difference should be about 100 kV/cm. The

fact that the predicted difference in the fields in Si is small compared to the predicted differences in the other two materials with the fact that the lock-on effect has never been experimentally observed in Si.

7.7 Results For Gallium Phosphide (GaP)

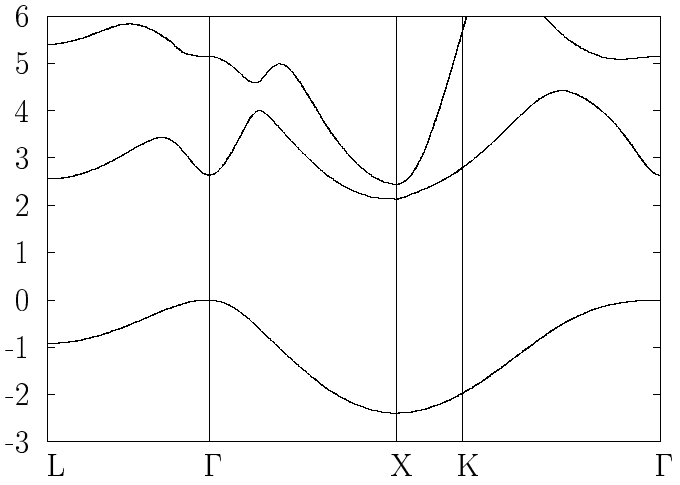

Figure 7.27: GaP bandstructure plot.

The bandstructure used in the simulations for GaP is shown in Fig. 7.27. It contains two conduction bands and one valence band. It was calculated using the local empirical pseudopotential method [64], along with the form factors of Cohen and Bergstresser [64]. The GaP parameters used in the calculations are shown in Table 7.5.

The calculated impact ionization and Auger rate coefficients for GaP are shown in Figs. 7.28 and 7.29, respectively. The impact ionization coefficients can be fit to an exponential function of F^{-1} and the Auger rate coefficients depend linearly on F. Thus Eq. 7.1 can be used to fit the results without cc-scattering and predict F_B =192 kV/cm. For these calculations, the defect recombination rate r was set to $r = 1 \times 10^6 s^{-1}$. The value of r, which is lower than in all the other materials, was chosen so that F_B would be approximately 200 kV/cm. This allows us to make a more direct comparison to GaAs and InP results.

Number of particles in cond. and val. band	100
Lattice constant, a_{lat}	5.44
Mass density, ρ	4.14 g/cm^3
Speed of sound, v_s	5.84×10^5 cm/s
Acoustic deformation potential, D_a	5.0 eV
Optical deformation potential, D_0	1.0×10^8 eV/cm
Opt. def. phonon energy, $\hbar\omega_0$	0.045 eV
Polar optical phonon energy, $\hbar\omega_{po}$	0.045 eV
ϵ_0	11.10
ϵ_{inf}	9.08

Table 7.5: Simulation parameters for GaP

It has been surprisingly difficult to find a good value for the intrinsic breakdown field of GaP. The only breakdown work found involves junction breakdown [72] instead of intrinsic breakdown, which results in a higher breakdown fields. In spite of this,

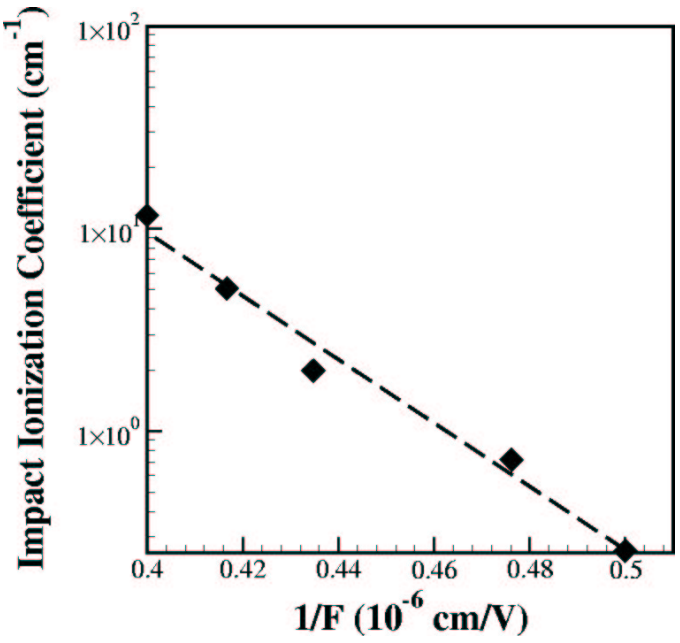

Figure 7.28: The impact ionization coefficient α as a function of inverse field for GaP.

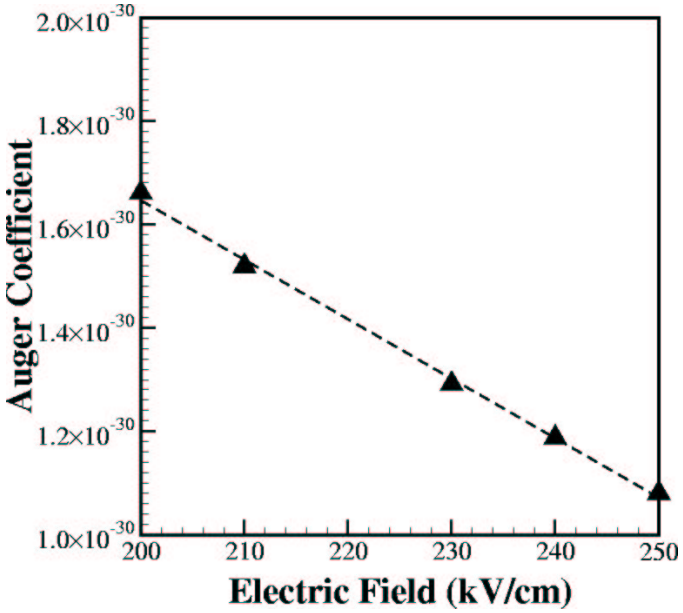

Figure 7.29: The Auger rate coefficient, a, as a function of field for GaP.

there is little doubt that InP would have a much higher experimental breakdown field than the theoretical value calculated. As noted above, the value chosen for r is two orders of magnitude smaller than that for the other materials. It is worth remembering that while the lock-on and breakdown fields depend strongly upon r, the difference between the two $(F_B - F_{LO})$ is not strongly dependent on r. This means that while the intrinsic breakdown field calculated would probably not match experimental breakdown fields, it is still reasonable to conclude that the lock-on field and the intrinsic breakdown field will be close to one another regardless of the value of breakdown field.

The distribution function, near the calculated breakdown field, can offer some insight into whether or not to expect a large difference between the lock-on field and the intrinsic breakdown field. Figure 7.30 shows the EMC calculated distribution function without cc-scattering (solid curve) for $F = 200\ kV/cm$, along with an approximate Maxwellian distribution (dashed curve), and the band gap of the GaP bandstructure (the dotted vertical line). Figure 7.30 suggests very little difference in the impact ionization rate will be created by going from the EMC distribution

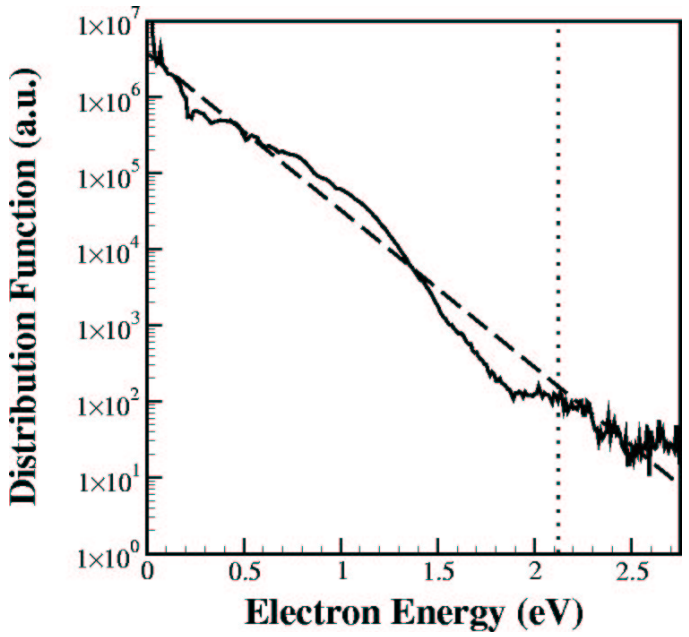

Figure 7.30: The distribution function as a function of carrier energy for GaP when F=200 kV/cm. The solid curve is the EMC distribution function without cc-scattering, and the dashed curve is an approximate Maxwellian distribution. The dotted line marks the energy gap of 2.120 eV.

without cc-scattering to the Maxwellian distribution, thus the lock-on field should be close to the breakdown field.

The breakdown plot for GaP is shown in Fig. 7.31. As noted above, the EMC calculations without cc-scattering predict an intrinsic breakdown field F_B for GaP of 192 kV/cm. The EMC results with cc-scattering predict a lock-on field F_{LO} of approximately 176 kV/cm. This means the predicted difference between F_B and F_{LO} is 16 kV/cm. It is worth noting that, the EMC calculations with cc-scattering for GaP actually produce a lower lock-on field than the Maxwellian results do; this is similar to the results for Si.

As noted in the discussion of lock-on, an experimental effort was made to determine if GaP would show evidence of lock-on given the similarity of bandstructure to GaAs and InP. The experimental results show that GaP does not exhibit lock-on [26]

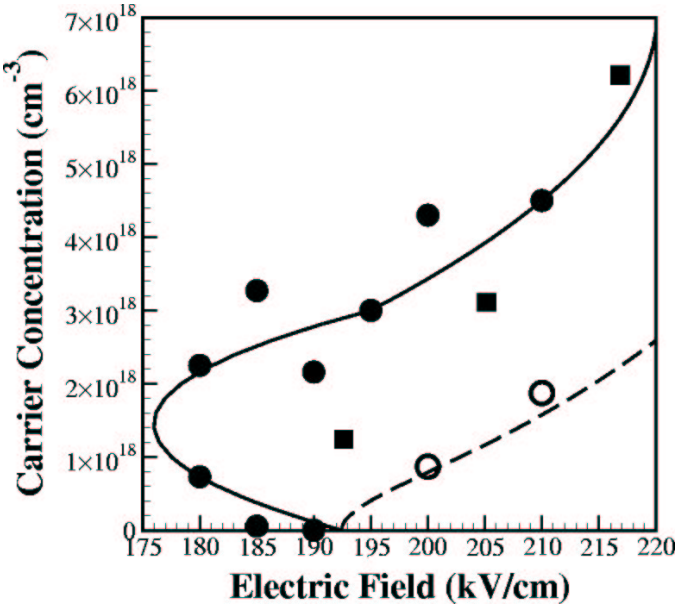

Figure 7.31: Breakdown plot for GaP.

in agreement with the EMC results that suggest experimental observation of lock-on in GaP would be very difficult.

CHAPTER VIII
CONCLUSIONS

This research was motivated initially by a desire to obtain a theoretical explanation of the lock-on effect in photoconductive semiconductor switches (PCSS's). However, as the work progressed, a theory developed which not only qualitatively explains the existence of lock-on current filaments, but also gives new insight into the old problem of electrical breakdown in insulators. This new theory uses a rate equation approach and an assumption that electrical breakdown is a high field, steady state condition to examine the electric field and carrier density dependence of breakdown. The steady state assumption views breakdown as a competition between impact ionization, Auger recombination, and defect recombination, each of which is included in this calculations. Using this method, predictions for both a lock-on field and an intrinsic or bulk breakdown field can be obtained.

The foundation for this work is the collective impact ionization theory which shows that, at high carrier densities, the presence of carrier-carrier scattering increases the impact ionization probability at a given field, causing electrical breakdown to occur at fields below the intrinsic breakdown field. Most other electrical breakdown theories focus exclusively on the the electric field dependence of the impact ionization rate coefficient.

In this approach, this traditional view of breakdown is expanded to include both the field and the carrier density dependence of the impact ionization rate. The carrier density dependence of this rate explains the sudden increase in carrier density associated with intrinsic breakdown. Along with the steady state assumption, this dependence also predicts that for some fields below the intrinsic breakdown field there are two stable steady state carrier densities which can coexist and one unstable steady state. The first stable steady steady state is when the carrier density is zero, this corresponds to the off state for a PCSS. The unstable steady state represents the carrier density which must be injected in order to trigger the switch into the lock-on

state. The final steady state, at high densities, is also a stable state. It is this low field, high density form of breakdown which gives rise to the lock-on effect in PCSS's and the coexistence of the two stable states which explains the existence of lock-on current filaments. This theory thus shows, for the first time, that the lock-on effect is a special case of electrical breakdown. In fact, based upon the results of this research, the lock-on effect is the experimental observation which confirms the existence of the predicted low field, high carrier density electrical breakdown phenomenon.

This theory has been implemented using two types of ensemble Monte Carlo (EMC) methods to calculate the distribution functions. To simulate cases where the carrier density is low, EMC calculations without including cc-scattering have been used. For cases where the carrier density is high, so that carrier-carrier scattering must be included and where this scattering is significant, an Ensemble Monte Carlo (EMC) approach including the effects of cc-scattering has been used. The phonon scattering mechanisms and rates used in the EMC calculations are discussed in Appendix A and are also discussed in more detail in Samsoo Kang's PhD dissertation [11]. From the resulting distribution function, the impact ionization and Auger recombination rates were calculated. Practical difficulties in implementing the EMC method including cc-scattering at some fields and at high carrier densities led us to also approximate the steady state, high density distribution function as a Maxwellian distribution. The Maxwellian distribution function was compared to the EMC distribution function without cc-scattering.

The primary results of this work are summarized in breakdown plots, which are discussed in detail in previous chapters. (In particular see figures 7.1, 7.11, 7.15, 7.21., 7.25, 7.31.) These plot the electric field and carrier density dependence of the steady state rate of change of carrier density in the EMC without cc-scattering, the EMC with cc-scattering, and the Maxwellian approximations. In order to test the approach, calculations were first performed for two different model materials, in which the conduction and valence bands were assumed to be parabolic. Then calculations for GaAs, InP, Si, and GaP were preformed using electronic energy bands computed

in the local empirical pseudopotential approximation [64].

The breakdown plots for the various materials allow us to qualitatively and quantitatively define, and to make predictions of both the intrinsic breakdown field and the lock-on field in each of the materials considered. The plots also explain the existence of lock-on current filaments. To our knowledge, this is the first theory to make predictions for both of these electric fields in GaAs and InP, and the only to include Si and GaP.

These results support the conclusion that there will be a sudden increase in carrier density when the applied field exceeds the intrinsic breakdown field only if the impact ionization rate is enhanced by increasing carrier density. Any other effect which results in a carrier density dependence will also produce an effect similar to lock-on. Some initial calculations were done for band gap narrowing in silicon [73], which resulted in a similar effect.

Each of the materials studied in this research (GaAs, InP, Si, and GaP) have breakdown plots which show similar qualitative behavior. The predictions for the lock-on and breakdown fields for these materials are summarized in Table 8.1. As mentioned above, these are (to our knowledge) the first predictions of intrinsic breakdown fields in Si and GaP. The lock-on field predictions in GaAs and InP, in which the lock-on effect has been observed, are considerably higher than the experimental lock-on fields. These predictions are clearly in error quantitatively. The reasons for this

Material	F_{LO} (th) (kV/cm)	F_B (th) (kV/cm)	F_{LO} (exp) (kV/cm)	F_B (exp) (kV/cm)
GaAs	90	177	3.5-9.5 [8]	143 [8, 4]
InP	40	173	14.4 [24]	130 [71]
Si	77	104	not observed [18]	91 [8, 4]
GaP	176	192	not observed [26]	-

Table 8.1: Theoretical (th) and experimental (exp) lock-on and breakdown fields

theoretical-experimental discrepancy are not known. It may be due to other effects which increase the impact ionization rates dependence on carrier density. It is also worth noting that r could easily be treated as a fitting parameter in this analysis. The breakdown fields for GaAs and InP are larger than the experimental values. Better matching for the breakdown field could be obtained by decreasing r, this would also decrease the lock-on field. It is worth noting that, since in this approach, lock-on is a special case of a field and density dependent electrical breakdown, lock-on fields in Si and GaP are also predicted, which are materials in which this effect has not been observed.

From the viewpoint of this theory, there are two primary differences between the materials in which lock-on has been observed (GaAs and InP) and those in which it has not (Si and GaP). The first difference is the obvious one that GaAs and InP are direct bandgap materials while Si and GaP have indirect bandgaps. The second difference, which may be correlated with the first, concerns the predicted differences between the intrinsic breakdown field and the lock-on field in these materials. For GaAs and InP, the predict difference $F_B - F_{LO}$ is 87 and 133 kV/cm respectively, while in Si and GaP, this difference is much smaller, of the order of 27 kV/cm in Si and 16 kV/cm in GaP. A reason that this effect has not been observed in these materials may thus be that the lock-on effect occurs at fields sufficiently close to the intrinsic breakdown field that it would be difficult to distinguish experimentally from intrinsic breakdown.

As has been discussed, theoretically, this difference depends on how Maxwellian the distribution function is when only phonon scattering is included. If this function is already very nearly Maxwellian (as in Si and GaP), then there will be little enhancement of the impact ionization rate when cc-scattering is included in the EMC calculations and the two fields will therefore be close to each other. However, if the phonon-only distribution is very non-Maxwellian (as in GaAs and InP), then when cc-scattering is included, the impact ionization rate is expected to be significantly enhanced and thus the two fields will be far apart.

Future work in this project could include the following: Doing calculations for other materials of possible interest in PCSS research, including SiC or GaN. Altering the code so that it calculates r directly for the material based on the carrier distribution function. This change would help eliminate the major adjustable parameter. Greater research to understanding why InP and GaAs are strongly effected by the inclusion of cc-scattering and Si and GaP do not. Such research would focus on the causes of a Maxwellian distribution in the absence of cc-scattering. Better understanding of this more fundamental issue might allow for the engineering of materials to either eliminate or even cause the lock-on effect.

BIBLIOGRAPHY

[1] D. H. Auston: *Appl. Phys. Lett.* **26** (1975) 101

[2] M. D. Pocha, W. W. Hofer: *chapt. 3, High-Power Optically Activated Solid State Switches*, p. 43: Artech House, Boston (1994)

[3] G. Loubriel, F. J. Zutavern, H. Hjalmarson, M. W. O'Malley: In: *Proc. 7th IEEE Pulsed Power Conf., Monteray, CA*, p. 365, New York (1989). Institute of Electrical and Electronics Engineers, Inc.

[4] G. M. Loubriel, M. W. O'Malley, F. J. Zutavern: In: *Proc. 6th IEEE Pulsed Power Conf., Arlington, VA*, p. 145, New York (1987). Institute of Electrical and Electronics Engineers, Inc.

[5] F. J. Zutavern, M. W. O'Malley, G. M. Loubriel: In: *Proc. 6th IEEE Pulsed Power Conf., Arlington, VA*, p. 577, New York (1987). Institute of Electrical and Electronics Engineers, Inc.

[6] M. Mazzola, K. Schoenbach, V. K. Lakdawala, R. Germer, G. Loubriel, F. J. Zutavern: *Appl. Phys. Lett.* **54** (1989) 742

[7] R. L. Druce, K. L. Griffin, W. W. Hofer, M. D. Pocha: In: *Proc. Optically and Electron-beam Controlled Semiconductor Switches Workshop, Norfolk, VA* (1998)

[8] F. J. Zutavern, G. M. Loubriel: *chapt. 11, High-Power Optically Activated Solid State Switches*, p. 245: Artech House, Boston (1994)

[9] H. P. Hjalmarson, F. J. Zutavern, G. M. Loubriel, A. Baca, K. Khachaturyan, D. R. Wake: *An impact ionization model for optically-triggered current filaments in gaas*: Tech. Rep. Sandia Report SAND93-3972, Sandia National Laboratories (1996)

[10] H. Hjalmarson, G. Loubriel, F. Zutavern, D. Wake, S. Kang, K. Kambour, C. Myles: In: *Proc. 12th IEEE Pulsed Power Conference, Monterey, CA*, p. 299, New York (1999). Institute of Electrical and Electronics Engineers, Inc.

[11] S. Kang: *Simulation of High Field Transport in Photoconductive Semiconductor Switches*: Ph.D. thesis, Texas Tech University (1998)

[12] R. Brinkman, K. Schoenbach, D. Stoudt, V. K. Lakdawala, G. Erdin, M. Kennedy: *IEEE Trans. Elect. Dev.* **38** (1991) 701

[13] M. Weiner, A. Kim: *chapt. 10, High-Power Optically Activated Solid State Switches*, p. 220: Artech House, Boston (1994)

[14] W. C. Nunnally, R. B. Hammond: *chapt. 12 Picosecond Optoelectronic Devices*, p. 388: Academic Press, Orlando, Fla (1984)

[15] W. C. Nunnally: *chapt. 2, High-Power Optically Activated Solid State Switches*, p. 37: Artech House, Boston (1994)

[16] J. H. Hur, P. Hadizad, S. R. Hummel, P. D. Dapkus, H. R. Fetterman, M. A. Gunderson: *IEEE Trans. Elect. Dev.* **37** (1990) 2520

[17] K. Schoenbach, V. K. Lakdawala, D. C. Stoudt, T. F. Smith, R. Brinkman: *IEEE Trans. Elect. Dev.* **36** (1989) 1793

[18] G. Loubriel, M. W. O'Malley, F. J. Zutavern, B. B. McKenzie, W. R. Conley, H. P. Hjalmarson: In: *Proc. 18th IEEE Power Modulator Symposium, Hilton Head, SC*, p. 312, New York (1988). Institute of Electrical and Electronics Engineers, Inc.

[19] F. J. Zutavern, G. M. Loubriel, M. W. O'Malley, W. D. Helgeson, D. L. McLaughlin: In: *Proc. 8th IEEE Pulsed Power Conference, San Diego, CA*, p. 23, New York (1991). Institute of Electrical and Electronics Engineers, Inc.

[20] R. A. Falk, J. C. Adams, G. L. Bohnhoff-Hlavecek: In: *Proc. 8th IEEE Pulsed Power Conference, San Diego, CA*, p. 29, New York (1991). Institute of Electrical and Electronics Engineers, Inc.

[21] F. J. Zutavern, G. Loubriel, M. W. O'Malley, W. Helgeson, D. McLaughlin, G. J. Denison: In: *Proc. 20th IEEE Power Modulator Symposium, Myrtle Beach, SC*, p. 305, New York (1992). Institute of Electrical and Electronics Engineers, Inc.

[22] F. J. Zutavern, G. Loubriel, W. Helgeson, M. W. O'Malley, R. R. Gallegos, A. G. Baca, T. A. Plut, H. P. Hjalmarson: In: *Proc. 21st IEEE Power Modulator Symposium, Costa Mesa, CA*, p. 116, New York (1994). Institute of Electrical and Electronics Engineers, Inc.

[23] F. J. Zutavern, G. M. Loubriel, A. Mar, M. W. O'Malley, A. G. Baca, M. J. Hafich, G. A. Vawter, W. W. Chow, H. P. Hjalmarson: *Current filament semiconductor lasers (cfsl)*: Tech. Rep. Sandia Report SAND2001-0963, Sandia National Laboratories (2001)

[24] F. J. Zutavern, G. Loubriel, M. W. O'Malley, L. P. Shanwald, W. D. Helgeson, D. L. McLaughlin, B. B. McKenzie: *IEEE Trans. Elect. Dev.* **37** (1990) 2472

[25] R. Brinkman, K. Schoenbach: In: *Proc. 8th IEEE Pulsed Power Conference, San Diego, CA*, p. 94, New York (1991). Institute of Electrical and Electronics Engineers, Inc.

[26] G. Loubriel, F. J. Zutavern, G. J. Denison, W. Helgeson, D. McLaughlin, M. W. O'Malley, H. P. Hjalmarson: In: *Proc. 9th IEEE Pulsed Power Conference, Albuquerque, NM*, p. 76, New York (1993). Institute of Electrical and Electronics Engineers, Inc.

[27] R. Joshi, J. Kenney, K. Schoenbach, W. Hofer: *J. Appl. Phys.* **72** (1992) 4781

[28] A. G. Baca, H. P. Hjalmarson, G. Loubriel, D. McLaughlin, F. J. Zutavern: In: *Proc. 9th IEEE Pulsed Power Conference, Albuquerque, NM*, p. 84, New York (1993). Institute of Electrical and Electronics Engineers, Inc.

[29] F. J. Zutavern, A. G. Baca, W. Helgeson, H. P. Hjalmarson, G. Loubriel, D. McLaughlin, M. W. O'Malley: In: *Proc. 9th IEEE Pulsed Power Conference, Albuquerque, NM*, p. 80, New York (1993). Institute of Electrical and Electronics Engineers, Inc.

[30] D. Stoudt, R. A. Rousch, M. G. Grothaus, A. M. Balekdjian, , R. J. Zeto: In: *Proc. 20th IEEE Power Modulator Symposium, Myrtle Beach, SC*, p. 245, New York (1992). Institute of Electrical and Electronics Engineers, Inc.

[31] M. Loubriel, F. J. Zutavern, A. Mar, A. G. Baca, H. P. Hjalmarson, M. W. O'Malley, G. J. Denison, W. Helgeson: In: *Proc. 23rd IEEE Power Modulator Symposium, Rancho Mirage and CA*, p. 101, New York (1998). Institute of Electrical and Electronics Engineers, Inc.

[32] G. M. Loubriel, F. J. Zutavern, A. Mar, M. W. O'Malley, W. Helgeson, D. J. Brown, H. P. Hjalmarson, A. G. Baca: In: *Proc. 11th IEEE Pulsed Power Conference, Baltimore, MA*, p. 405, New York (1997). Institute of Electrical and Electronics Engineers, Inc.

[33] A. Mar, G. Loubriel, F. J. Zutavern, M. W. O'Malley, W. Helgeson, D. J. Brown, H. P. Hjalmarson, A. G. Baca, R. L. Thornton, R. D. Donaldson: In: *Proc. 12th IEEE Pulsed Power Conference, Monterey, CA*, p. 303, New York (1999). Institute of Electrical and Electronics Engineers, Inc.

[34] A. Mar, G. Loubriel, F. J. Zutavern, M. W. O'Malley, W. Helgeson, D. J. Brown, H. P. Hjalmarson, A. G. Baca, R. L. Thornton, R. D. Donaldson: In: *Proc. 24th IEEE Power Modulator Symposium, Norfolk, VA*, p. 69, New York (2000). Institute of Electrical and Electronics Engineers, Inc.

[35] F. J. Zutavern, G. Loubriel, H. P. Hjalmarson, A. Mar, W. Helgeson, M. W. O'Malley, M. H. Ruebush: In: *Proc. 11th IEEE Pulsed Power Conf., Baltimore, MA*, p. 959, New York (1997). Institute of Electrical and Electronics Engineers, Inc.

[36] K. Schoenbach, V. Lakdawala, S. Ko, M. Mazzola, D. Stoudt, , T. Smith: In: *Proc. 18th IEEE Power Modulator Symposium, Hilton Head, SC*, p. 318, New York (1988). Institute of Electrical and Electronics Engineers, Inc.

[37] M. S. Mazzola, K. H. Schoenbach, V. K. Lakdawala, S. T. Ko: In: *Proc. 7th IEEE Pulsed Power Conf., Monteray, CA*, p. 418, New York (1989). Institute of Electrical and Electronics Engineers, Inc.

[38] D. C. Stoudt, R. P. Brinkmann, R. A. Roush, M. S. Mazzola, F. J. Zutavern, G. Loubriel: In: *Proc. 9th IEEE Pulsed Power Conference, Albuquerque, NM*, p. 72, New York (1993). Institute of Electrical and Electronics Engineers, Inc.

[39] L. Partain, D. Day, R. Powell: *J. Appl. Phys.* **74** (1993) 335

[40] R. Brinkman, K. Schoenbach, D. Stoudt, V. Lakdawala, G. Gerdin, M. Kennedy: *IEEE Trans. Elect. Dev.* **38** (1991) 701

[41] R. P. Brinkman, K. H. Schoenbach, D. C. Stoudt, R. A. Roush: *SPIE* **1873** (1993) 192

[42] R. P. Brinkman: *J. Appl. Phys.* **68** (1990) 318

[43] H. Zhao, P. Hadizad, J. Hur, M. A. Gunderson: *J. Appl. Phys.* **73** (1993) 1807

[44] M. A. Gundersen, J. H. Hur, H. Zhao, C. W. Myles: *J. Appl. Phys.* **71** (1992) 3036

[45] C. D. Capps, R. A. Falk, J. C. Adams: *J. Appl. Phys.* **74** (1993) 6645

[46] G. Loubriel, F. J. Zutavern, H. P. Hjalmarson, R. Gallegos, W. Helgeson, M. O'Malley: *Appl. Phys. Lett.* **64** (1994) 3323

[47] G. Loubriel, F. J. Zutavern, M. W. O'Malley, R. R. Gallegos, W. Helgeson, H. P. Hjalmarson, A. G. Baca, T. A. Plut: In: *Proc. 21st IEEE Power Modulator Symposium, Costa Mesa, CA*, p. 120, New York (1994). Institute of Electrical and Electronics Engineers, Inc.

[48] J. O'Dwyer: *The Theory of Dielectric Breakdown of Solids*: Oxford University Press, London (1964)

[49] A. V. Hippel: *J. Appl. Phys.* **8** (1937) 815

[50] H. B. Callen: *Phys. Rev.* **76** (1949) 1394

[51] H. Fröhlich: *Proc. Roy. Soc. Lond. A* **160** (1937) 230

[52] H. Fröhlich: *Proc. Roy. Soc. Lond. A* **172** (1939) 94

[53] H. Fröhlich, B. V. Paranjape: *Proc. Phys. Soc. London B* **69** (1955) 21

[54] F. Seitz: *Phys. Rev.* **76** (1949) 1376

[55] K. G. McKay: *Phys. Rev.* **94** (1954) 877

[56] E. M. Conwell: *High Field Transport in Semiconductors*: Academic Press, New York (1967)

[57] A. R. Beattie, P. T. Landsberg: *Proc. Phys. Soc. A* **249** (1959) 16

[58] P. A. Wolff: *Phys. Rev.* **95** (1954) 1415

[59] G. A. Baraff: *Phys. Rev.* **128** (1962) 2507

[60] B. Davydov: *Phys. Rev.* **64** (1943) 156

[61] C. Moglestue: *Monte Carlo Simulation of Semiconductor Devices*: Chapman and Hall, London and New York (1993)

[62] T. Kurosawa: *Proceedings of the International Conference on the Physics of Semiconductors, Kyoto, J. Phys. Soc. Jap. Suppl.* **21** (1966) 424

[63] H. Rees: *J. Phys. Chem. Solids* **30** (1969) 645

[64] M. Cohen, T. Bergstresser: *Phys. Rev.* **141** (1969) 789

[65] T. Kunikiyo, M. Takenaka, Y. Kamakura, M. Yamaji, H. Mizuno, M. Morifuji, K. Taniguchi, C. Hamaguchi: *J. Appl. Phys.* **75** (1994) 297

[66] J. Bude, K. Hess: *J. Appl. Phys.* **72** (1992) 3554

[67] H. K. Jung, K. Taniguchi, C. Hamaguchi: *J. Appl. Phys.* **79** (1996) 2473

[68] M. V. Fischetti: *IEEE Trans. Elect. Dev.* **38** (1991) 634

[69] F. J. Zutavern, G. M. Loubriel: *chapt. 4, High-Power Optically Activated Solid State Switches*, p. 61: Artech House, Boston (1994)

[70] W. T. White III, C. G. Dease, M. D. Pocha, G. H. Khanaka: *IEEE Trans. Elect. Dev.* **37** (1990) 2532

[71] B. K. Ridley: *J. Appl. Phys.* **48** (1977) 754

[72] S. M. Sze, G. Gibbons: *Appl. Phys. Lett.* **85** (1966) 111

[73] E. K. Banghart, J. L.Gray: *IEEE Trans. Elect. Dev.* **39** (1992) 1108

[74] L. Reggiani: *Hot-Electron Transport in Semiconductors*: Springer Verlag, Heidelberg (1985)

[75] C. Jacoboni, L. Reggiani: *Rev. Mod. Phys.* **55** (1983) 645

[76] N. Takenaka, M. Inoue, Y. Inushi: *J Phys Soc Jpn* **47** (1979) 861

APPENDIX A

PHONON SCATTERING IN THE MONTE CARLO CALCULATIONS

In an EMC simulation there are three major effects. The free flight due to the field, the carrier-carrier scattering rates dealt with in Appendix B, and the phonon scattering rates dealt with here.

For a carrier-phonon scattering process, the transition rate τ^{-1} for electron-phonon scattering of an electron in state k to state k' is given by Fermi's Golden Rule

$$\tau^{-1} = \frac{2\pi}{\hbar} \sum_{\vec{k},\vec{k'}} | < \vec{k}|H_{int}|\vec{k'} > |^2 f_k(1 - f_{k'})\delta(E_{k'} - E_k \mp E_{ph}) \tag{A.1}$$

where $< \vec{k}|H_{int}|\vec{k'} >$ is the matrix element of the electron phonon Hamiltonian, E_{ph} is the phonon energy, f_k and $f_{k'}$ are the k-space distribution function values for states k and k' respectively, and E_k and $E_{k'}$ are the energies corresponding to states k and k'. Using the standard definition of the scattering rate $\lambda(\vec{k})$ it is possible to write the transition rate as the sum over $\vec{k}$ of the scattering rates.

$$\tau^{-1} = \sum_{\vec{k}} \lambda(\vec{k}) f_k \tag{A.2}$$

Comparing the two equations one gets

$$\lambda(\vec{k}) = \frac{2\pi}{\hbar} \sum_{\vec{k'}} | < \vec{k}|H_{int}|\vec{k'} > |^2 (1 - f_{k'})\delta(E_{k'} - E_k \mp E_{ph}). \tag{A.3}$$

According Eq. 6.4, the total scattering rate can be written as a sum of the quantum mechanical scattering rates $S_i(\vec{k}, \vec{k'})$. Using the fact that $E_{ph} = \hbar\omega_i$, this yields

$$S_i(\vec{k}, \vec{k'}) = \frac{2\pi}{\hbar} | < \vec{k}|H_i|\vec{k'} > |^2 (1 - f_{k'})\delta(E_{k'} - E_k \mp \hbar\omega_i). \tag{A.4}$$

To summarize, Eq. (A.4) describes the probability that an electron with a wave vector $\vec{k}$ with energy E_k is scattered by a phonon with energy $\hbar\omega_i$ to a state with wave vector $\vec{k'}$ and energy $E_{k'}$. The plus and minus signs correspond to the absorption

and emission of a phonon, respectively. f_k is the carrier distribution function and $< \vec{k}|H_i|\vec{k'} >$ is the matrix element of the electron-phonon interaction Hamiltonian for phonon scattering type i.

At this point, it becomes necessary to account for the finite nature of the k-space grid used in implementing the calculation. So instead of the computer code calculating the probability that an electron with wave vector $\vec{k}$ is scattered by a phonon to a state with wave vector $\vec{k'}$, it calculates the probability that an electron with wave vector $\vec{k}$ is scattered by a phonon into a state within a small k-space cube. This would mean changing the sums to sums over the cube k'_c, so

$$\lambda_i(\vec{k}) = \sum_{\vec{k_c}} S_i(\vec{k}, \vec{k_c}), \tag{A.5}$$

and within the cube

$$S_i(\vec{k}, \vec{k_c}) = \frac{2\pi}{\hbar} \sum_{k'} | < \vec{k}|H_i|\vec{k'} > |^2 (1 - f_{k'}) \delta(E_{k'} - E_k \mp \hbar\omega_i). \tag{A.6}$$

The definition of the density of states is

$$D(E) = \sum_{k'} \delta(E - E_{k'}). \tag{A.7}$$

A similar definition is possible for the density of states within a cube, where

$$D(E) = \sum_{k_c} D_{k_c}(E) = \sum_{k_c} \sum_{k'} \delta(E - E_{k'}). \tag{A.8}$$

If the matrix element is a constant within the cube, then it can be written

$$S_i(\vec{k}, \vec{k_c}) = \frac{2\pi}{\hbar} | < \vec{k}|H_i|\vec{k'} > |^2 (1 - f_{k'}) D_{k_c}(E_k \mp \hbar\omega_i). \tag{A.9}$$

If the code determines that a phonon scattering event has occurred, it then finds a point within the cube with the correct energy, and places the carrier there.

The square of the matrix element can be derived using Bloch wave functions for the carrier eigenstates, and it has the form [74]

$$| < \vec{k}|H_i|\vec{k'} > |^2 = |V(\vec{q})|^2 I^2, \tag{A.10}$$

where q is the momentum exchange ($\vec{q} = \vec{k_f} - \vec{k_i}$), $|V(\vec{q})|^2$ contains the q dependence of the matrix element, and I is overlap integral between states $|\vec{k} >$ and $|\vec{k'} >$. The overlap integral depends on the symmetries of the interaction and the Bloch functions of the initial and final states. Even though this is strictly less than one when non-parabolicity of the bands and other effects are included, $I = 1$ is used for simplicity.

There are three electron-phonon scattering processes included in this calculations: optical deformation potential scattering (op), acoustic deformation potential scattering (ac), and polar optical scattering (po).

A.1 Optical Deformation Potential scattering

The matrix element for the optical deformation potential scattering is given by (see for example [56, 74].)

$$|V(\vec{q})|^2 = \frac{D_o^2 \hbar}{2\rho V \omega_o}(n + \frac{1}{2} \pm \frac{1}{2}), \tag{A.11}$$

where D_o is the optical deformation potential and ρ is the density of the material. Therefore, the scattering rate becomes

$$S_{op}(\vec{k}, \vec{k_c}) = \frac{D_o^2 \pi}{\rho V \omega_o} D_{k_c}(E_k \mp \hbar\omega_o)(1 - f_{k'})(n + \frac{1}{2} \pm \frac{1}{2}). \tag{A.12}$$

A.2 Polar Optical Phonon Scattering

In polar materials, oppositely charged atoms have some vibrational modes which cause long-range electric fields in addition to deformation potentials. The interaction of the carriers with these fields produces additional types of scattering. As with the other scatterings, the matrix element is easily obtained. It is

$$|V(\vec{q})|^2 = \frac{e^2 \hbar \omega_{po}}{2\rho V \epsilon_p q^2}(n + \frac{1}{2} \pm \frac{1}{2}), \tag{A.13}$$

where $\frac{1}{\epsilon_p} = \frac{1}{\epsilon_\infty} - \frac{1}{\epsilon_0}$ and ϵ_∞ and ϵ_0 are dielectric constants for high and low frequencies respectively. Then the scattering rate is

$$S_{po}(\vec{k}, \vec{k_c}) = \frac{e^2 \pi \omega_{po}}{\rho V \epsilon_p} \frac{1}{q^2} D_{k_c}(E_k \mp \hbar\omega_{po})(1 - f_{k'})(n + \frac{1}{2} \pm \frac{1}{2}). \tag{A.14}$$

A.3 Acoustic Deformation Potential Scattering

The matrix element for acoustic deformation potential scattering is

$$|V(\vec{q})|^2 = \frac{D_a^2 \hbar q}{2\rho V v_s}(n + \frac{1}{2} \pm \frac{1}{2}), \tag{A.15}$$

where v_s is the sound velocity, and D_a is the acoustic deformation potential.

This makes the acoustic deformation scattering rate

$$S_{ac}(\vec{k}, \vec{k_c}) = \frac{2\pi}{\hbar} \frac{D_a^2 \hbar q}{2\rho V v_s}(n + \frac{1}{2} \pm \frac{1}{2}) D_{k_c}(E_k \mp \hbar\omega)(1 - f_{k'})(n + \frac{1}{2} \pm \frac{1}{2}). \tag{A.16}$$

APPENDIX B
CARRIER-CARRIER SCATTERING IN THE ENSEMBLE MONTE CARLO CALCULATIONS

The screened carrier-carrier interaction scattering rate for an electron with wavevector k_i can be written according to Fermi's Golden Rule as a sum over the possible other initial states, $k_{i'}$, and the possible final states, k_f and $k_{f'}$. The various wavevectors are 3-D vectors, however, to make the derivation easier to follow the vector symbols are not included. The screened carrier-carrier interaction scattering rate has the form

$$\begin{aligned}\lambda(k_i) &= \frac{2\pi}{\hbar}\frac{E_H^2 a_B^2}{\epsilon^2}\frac{(4\pi)^2}{\Omega^2}\sum_{i'ff'}\frac{1}{(q_0^2+q^2)^2}f_{i'}(1-f_f)(1-f_{f'}) \\ &\quad \times\delta_{k_i+k_{i'}-k_f+k_{f'}}\delta(E_i+E_{i'}-E_f-E_{f'})\end{aligned} \tag{B.1}$$

where q is square of the momentum exchange ($q = k_f - k_i$), ϵ is the dielectric constant of the material, Ω is the crystal volume, a_B is the Bohr radius, and E_H is the Hartree energy.

Converting the sums to integrals results in

$$\begin{aligned}\lambda(k_i) &= \frac{2\pi}{\hbar}\frac{E_H^2 a_B^2}{\epsilon^2}\frac{(4\pi)^2}{\Omega^2}\frac{\Omega^2}{(2\pi)^6}\int d^3k_{i'}\int d^3k_f\int d^3k_{f'}\frac{1}{(q_0^2+q^2)^2} \\ &\quad \times f_{i'}(1-f_f)(1-f_{f'})\delta_{k_i+k_{i'}-k_f+k_{f'}}\delta(E_i+E_{i'}-E_f-E_{f'})\end{aligned} \tag{B.2}$$

$$\begin{aligned}&= \frac{4}{\hbar}\frac{E_H^2 a_B^2}{\epsilon^2}\frac{1}{(2\pi)^3}\int d^3k_{i'}\int d^3k_f\int d^3k_{f'}\frac{1}{(q_0^2+q^2)^2} \\ &\quad \times f_{i'}(1-f_f)(1-f_{f'})\delta_{k_i+k_{i'}-k_f+k_{f'}}\delta(E_i+E_{i'}-E_f-E_{f'})\end{aligned} \tag{B.3}$$

It is useful to convert to dimensionless wavevectors. Doing so and then simplifying results in

$$\lambda = c_0\int d^3\overline{k}_{i'}\int d^3\overline{k}_f f_{i'}(1-f_f)(1-f_{f'})\frac{1}{(\overline{q}_0^2+\overline{q}^2)^2}\delta(E_i+E_{i'}-E_f-E_{f'}) \tag{B.4}$$

with

$$c_0 = \frac{2}{\pi\hbar}\frac{E_H^2}{\epsilon^2}(\frac{a_B}{a})^2. \tag{B.5}$$

In Eq. B.4 the dimensionless wavevectors are defined by relations of the form:

$$k = \frac{2\pi}{a}\overline{k} \tag{B.6}$$

Assuming that $f_f << 1$ and $f_{f'} << 1$ Eq. B.4 can be approximated as

$$\lambda = c_0 \int d^3\overline{k}_{i'} f_{i'} \int d^3\overline{k}_f \frac{1}{(\overline{q}_0^2 + \overline{q}^2)^2}\delta(E_i + E_{i'} - E_f - E_{f'}) \tag{B.7}$$

one of the assumptions is that all the states are on the same parabolic effective mass band, therefore all the masses are the same. Thus the energy expression in the delta function becomes

$$\begin{aligned} E &= E_i + E_{i'} - E_f - E_{f'} \\ &= \frac{\hbar^2}{2m^*}(k_i^2 + k_{i'}^2 - k_i^2 - k_{i'}^2) \\ &= \frac{\hbar^2(2\pi)^2}{2m^*a^2}(\overline{k}_i^2 + \overline{k}_{i'}^2 - \overline{k}_i^2 - \overline{k}_{i'}^2) \end{aligned}$$

Furthermore

$$\frac{\hbar^2(2\pi)^2}{2m^*a^2} = \frac{E_H}{2(m^*/m)}\frac{(2\pi)^2 a_B^2}{a^2} \tag{B.8}$$

Using

$$\delta(\alpha x) = \frac{\delta(x)}{\alpha}, \tag{B.9}$$

the prefactor becomes

$$\begin{aligned} \overline{c}_0 &= \frac{2}{\pi\hbar}\frac{E_H^2}{\epsilon^2}(\frac{a_B}{a})^2\frac{2(m^*/m)}{E_H}\frac{a^2}{(2\pi)^2 a_B^2} \\ &= \frac{1}{\pi^3}\frac{E_H(m^*/m)}{\hbar\varepsilon^2} \end{aligned}$$

And Eq. B.7 becomes

$$\lambda = \overline{c}_0 \int d^3\overline{k}_{i'} f_{i'} \int d^3\overline{k}_f \frac{1}{(\overline{q}_0^2 + \overline{q}^2)^2} \delta(\overline{k}_i^2 + \overline{k}_{i'}^2 - \overline{k}_i^2 - \overline{k}_{i'}^2) \tag{B.10}$$

Now let

$$\begin{aligned} \overline{k}_f &= \overline{k}_i + \overline{q} \\ \overline{k}_{f'} &= \overline{k}_{i'} - \overline{q} \end{aligned}$$

Then

$$\begin{aligned} \overline{k}_i^2 + \overline{k}_{i'}^2 - \overline{k}_i^2 - \overline{k}_{i'}^2 &= \overline{k}_i^2 + \overline{k}_{i'}^2 - (\overline{k}_i + \overline{q})^2 - (\overline{k}_{i'} - \overline{q})^2 \\ &= \overline{g} \cdot \overline{q} - \overline{q}^2 \end{aligned}$$

in which

$$\overline{g} = \overline{k}_{i'} - \overline{k}_i \tag{B.11}$$

Using

$$\delta(\alpha x) = \frac{\delta(x)}{\alpha} \tag{B.12}$$

Then

$$\begin{aligned} \lambda &= \overline{c}_0 \int d^3\overline{k}_{i'} f_{i'} \int_0^\infty \int \frac{1}{(\overline{q}_0^2 + \overline{q}^2)^2} \delta(2\overline{g} \cdot \overline{q} - 2\overline{q}^2) \sin(\theta) d\theta \overline{q}^2 d\overline{q} \\ &= 2\pi \overline{c}_0 \int d^3\overline{k}_{i'} f_{i'} \int_0^\infty \frac{1}{2\overline{q}\overline{g}} \int \frac{1}{(\overline{q}_0^2 + \overline{q}^2)^2} \delta(\cos(\theta) - \overline{q}/\overline{g})) \sin(\theta) d\theta \overline{q}^2 d\overline{q} \\ &= \pi \overline{c}_0 \int d^3\overline{k}_{i'} f_{i'} \int_0^g \frac{1}{\overline{g}} \frac{1}{(\overline{q}_0^2 + \overline{q}^2)^2} \overline{q} d\overline{q} \end{aligned}$$

Note that the delta function restricts the range of q. The remaining integral is easy to perform. To be explicit, use

$$
\begin{aligned}
u &= \overline{q}_0^2 + \overline{q}^2 \\
du &= 2\overline{q}d\overline{q}
\end{aligned}
$$

then

$$
\begin{aligned}
\lambda &= \frac{\pi\overline{c}_0}{2}\int d^3\overline{k}_{i'} f_{i'} \frac{1}{\overline{g}} \int_{\overline{q}_0^2}^{\overline{q}_0^2+\overline{g}^2} \frac{du}{u^2} \\
&= \frac{\pi\overline{c}_0}{2}\int d^3\overline{k}_{i'} f_{i'} \frac{1}{\overline{g}} \left[\frac{1}{\overline{q}_0^2} - \frac{1}{\overline{q}_0^2+\overline{g}^2}\right] \\
&= \frac{\pi\overline{c}_0}{2}\int d^3\overline{k}_{i'} f_{i'} \frac{\overline{g}}{\overline{q}_0^2(\overline{q}_0^2+\overline{g}^2)}
\end{aligned}
$$

This is as far as the screened result goes, however if as discussed above one assumes a minimum momentum exchange, $\overline{q}_{min}$, and no screening that would change the integral to

$$\lambda = \pi\overline{c}_0 \int d^3\overline{k}_{i'} f_{i'} \int_{\overline{q}_{min}}^{g} \frac{1}{\overline{g}}\frac{1}{\overline{q}^4}\overline{q}d\overline{q} \tag{B.13}$$

Simplifying one gets

$$\lambda = \pi\overline{c}_0 \int d^3\overline{k}_{i'} f_{i'} \int_{\overline{q}_{min}}^{g} \frac{1}{\overline{g}}\frac{1}{\overline{q}^3}d\overline{q} = \frac{\pi\overline{c}_0}{2}\int d^3\overline{k}_{i'} f_{i'} \frac{1}{\overline{g}} \left[\frac{1}{\overline{q}_{min}^2} - \frac{1}{\overline{g}^2}\right] \tag{B.14}$$

In order to implement this in an EMC code, it is necessary to go from a result based on distribution function to a result based on specific particles which are at specific points in k-space, so a few changes need to be made. If there is possible scattering with N carriers each having dimensionless wavevector $\overline{k}_j$ then the integral over $\overline{k}_{i'}$ includes delta functions for however many carriers there are. So the equation becomes

$$\lambda = \frac{\pi\overline{c}_0}{2}\int d^3\overline{k}_{i'} [\frac{1}{N}\sum_{j=1}^{N} \delta(\overline{k}_{i'} - \overline{k}_j) f_j] \frac{1}{\overline{g}} \left[\frac{1}{\overline{q}_{min}^2} - \frac{1}{\overline{g}^2}\right] \tag{B.15}$$

Which can be rewritten as

$$\begin{aligned}\lambda &= \frac{\pi\overline{c}_0}{2N}\sum_{j=1}^{N}\int d^3\overline{k}_{i'}\delta(\overline{k}_{i'}-\overline{k}_j)f_j\frac{1}{\overline{g}}\left[\frac{1}{\overline{q}^2_{min}}-\frac{1}{\overline{g}^2}\right] \\ &= \frac{\pi\overline{c}_0}{2N}\sum_{j=1}^{N}f_j\frac{1}{\overline{g}}\left[\frac{1}{\overline{q}^2_{min}}-\frac{1}{\overline{g}^2}\right]\end{aligned}$$

Since the EMC code deals with specific particles then f_j does not depend on particle number, and is simply the value of occupancy assigned for each particle. This means

$$f_j = \frac{N}{n_{npc}} \tag{B.16}$$

where n_{npc} is the number of particles allowed in each of the small cubes.

Combining and simplifying one gets the total carrier-carrier scattering rate as

$$\lambda = \frac{\pi\overline{c}_0}{2n_{npc}}\sum_{j=1}^{N}\frac{1}{\overline{g}}\left[\frac{1}{\overline{q}^2_{min}}-\frac{1}{\overline{g}^2}\right] \tag{B.17}$$

Once it is determined that a carrier-carrier event happens and which carriers are involved the next step is to determine the angles θ and ϕ. To do this it is necessary to convert from the probability for a given angle $P(\theta)$ into a form which will allow us to use a random number to find θ once an event has occurred $\theta(r)$. This is done using the direct technique which is discussed on page 698 of Jacoboni and Reggiani [75].

The direct technique says that the relationship between the random number, r and the probability, $P(x)$ where x goes from a to b is

$$r = \frac{\int_a^{x_r} P(x)dx}{\int_a^b P(x)dx} \tag{B.18}$$

Solving this equation for x_r then gives us x_r as a function of r.

Following the methodology of Takenaka [76] one writes Eq. B.4 in terms of theta, assuming there is no screening i.e. $q_0 = 0$. This yields

$$\lambda = c_0 \int d^3\overline{k}_{i'} \int d^3\overline{k}_f f_{i'}(1-f_f)(1-f_{f'})\frac{1}{\overline{g}^4 cos^4(\theta)}\delta(E_i + E_{i'} - E_f - E_{f'}) \quad \text{(B.19)}$$

From this the probability can be written

$$P(\theta) = A\frac{sin(\theta)}{\overline{g}^4 cos^4(\theta)} \quad \text{(B.20)}$$

where A is a normalization constant and the $sin(\theta)$ comes from the integration using cylindrical coordinates.

The next step in this process is to define the limits of integration. Even though θ can go from 0 to π one can treat the limits as being from 0 to $\pi/2$ because the angles from $\pi/2$ to π are simply mirror images of the angles from 0 to $\pi/2$ where the only difference is that the particle labels are swapped. For example, the only difference between an event where $\theta = \pi/4$ and one where $\theta = 3\pi/4$ is which particle is labelled 1f and which is labelled 2f.

There is still one apparent problem here since if $\theta = \pi/2$ the probability would be infinite, but θ cannot be $\pi/2$. The limit on θ actually comes from the minimum wavevector change, $\overline{q}_{min}$, with θ_{max} defined by

$$\overline{q}_{min} = gcos(\theta_{max}) \quad \text{(B.21)}$$

Plugging this into Eq. B.18 gives

$$r = \frac{\int_0^{\theta_r} P(\theta)d\theta}{\int_0^{\theta_{max}} P(\theta)d\theta} = \frac{\int_0^{\theta_r} \frac{sin(\theta)}{cos^4(\theta)}d\theta}{\int_0^{\theta_{max}} \frac{sin(\theta)}{cos^4(\theta)}d\theta} \quad \text{(B.22)}$$

Since both integrals are the same, except for limits, there is only one intergal which can be evaluated as

$$\int \frac{sin(\theta)}{cos^4(\theta)}d\theta = -\int \frac{du}{u^4} = \frac{1}{3u^3} = \frac{1}{3cos^3(\theta)} \quad \text{(B.23)}$$

where $u = cos(\theta)$. Plugging this in results in

$$r = \frac{\frac{1}{cos^3(\theta_r)} - \frac{1}{cos^3(0)}}{\frac{1}{cos^3(\theta_{max})} - \frac{1}{cos^3(0)}} = \frac{\frac{1}{cos^3(\theta_r)} - 1}{\frac{g^3}{\overline{q}^3_{min}} - 1} == \frac{\frac{1}{cos^3(\theta_r)} - 1}{\frac{g^3 - \overline{q}^3_{min}}{\overline{q}^3_{min}}} \tag{B.24}$$

Cross multiplying gives

$$\frac{g^3 - \overline{q}^3_{min}}{\overline{q}^3_{min}} r = \frac{1}{cos^3(\theta_r)} - 1 \tag{B.25}$$

Solving for $cos(\theta_r)$ gives

$$cos(\theta_r) = \frac{1}{1 + \frac{g^3 - \overline{q}^3_{min}}{\overline{q}^3_{min}} r} \tag{B.26}$$

So $\theta(r)$ can be written as

$$\theta(r) = acos \left[\frac{1}{1 + \frac{g^3 - \overline{q}^3_{min}}{\overline{q}^3_{min}} r} \right] \tag{B.27}$$

Finding $\phi(r)$ is much simpler since $P(\phi) = A$ with the limits being from 0 to 2π. A straight forward calculation lets one write

$$\phi(r) = 2\pi r \tag{B.28}$$

APPENDIX C

IMPACT IONIZATION RATE TABLE CALCULATION

The total impact ionization rate for a given carrier distribution function can be written simply as the sum of the impact ionization rates for each k point in the grid, or mathematically

$$r_{ii} = \sum \lambda(k_i) f_{k_{i'}} \tag{C.1}$$

where

$$\begin{aligned} \lambda(k_i) &= \frac{2\pi}{\hbar}\frac{E_H^2 a_B^2}{\epsilon^2}\frac{(4\pi)^2}{\Omega^2}\sum_{i'ff'}\frac{|O_{if}|^2\,|O_{i'f'}|^2}{q^4} f_{i'}(1-f_f)(1-f_{f'}) \\ &\quad \times\delta_{k_i+k_{i'}-k_f+k_{f'}}\delta(E_i+E_{i'}-E_f-E_{f'}). \end{aligned} \tag{C.2}$$

The delta function removes one of the k-sums. The remaining sums can then be expressed as

$$\lambda(k_i) = \frac{2\pi}{\hbar}\frac{E_H^2 a_B^2}{\epsilon^2}\frac{(4\pi)^2}{\Omega^2}\sum_{i'f}\frac{|O_{if}|^2\,|O_{i'f'}|^2}{q^4} f_{i'}(1-f_f)(1-f_{f'})\delta(E_i+E_{i'}-E_f-E_{f'}). \tag{C.3}$$

It is useful to convert to dimensionless $\bar{k}$, where $\bar{k} = \frac{2\pi}{a}k$. This also means converting to dimensionless $\bar{q}$, where $\bar{q} = \frac{2\pi}{a}q$. Doing this and then simplify results in

$$\lambda(\bar{k}_i) = c_0(\frac{a^3}{V})^2\sum_{i'f}\frac{|O_{if}|^2\,|O_{i'f'}|^2}{\bar{q}^4} f_{i'}(1-f_f)(1-f_{f'})\delta(E_i+E_{i'}-E_f-E_{f'}) \tag{C.4}$$

where

$$c_0 = \frac{2}{\hbar}\frac{E_H^2}{\pi\epsilon^2}(\frac{a_B}{a})^2.$$

If the sum over all k_i' and k_f is converted into integrals, the result is

$$\lambda(\bar{k}_i) = c_0(\frac{a^3}{V})^2 \int_i \int_{'f} \frac{|O_{if}|^2 |O_{i'f'}|^2}{\bar{q}^4} f_{i'}(1-f_f)(1-f_{f'})\delta(E_i + E_{i'} - E_f - E_{f'}) d^3\bar{k}_{i'} d^3\bar{k}_f \tag{C.5}$$

But since the k-space grid is finite, it is possible to approximate the integrals as the sum of the integrals over the small cubes. Defining a quantity $S(k_i, k_{i'}, k_f, k_{f'})$ by the equation

$$\lambda(\bar{k}_i) = \sum_{k_{i'} k_f} S(k_i, k_{i'}, k_f, k_{f'}) f_{i'}(1-f_f)(1-f_{f'}) \tag{C.6}$$

then

$$S = \int_{cube_{k_{i'}}} \int_{cube_{k_f}} c_0 \frac{|O_{if}|^2 |O_{i'f'}|^2}{\bar{q}^4} d^3\bar{k}_{i'} d^3\bar{k}_f \delta(E_i + E_{i'} - E_f - E_{f'}) \tag{C.7}$$

In the histogram approximation, the δ function can be replaced by

$$\delta(E - E_{\bar{k}}) = \begin{cases} \frac{1}{\Delta} & \text{if } \mid E - E_{\bar{k}} \mid < \frac{\Delta}{2} \\ 0 & \text{otherwise} \end{cases} \tag{C.8}$$

Most of the S values will be zero. Assuming the overlaps are equal to one then those that are not will thus have the approximate value

$$S(k_i, k_{i'}, k_f, k_{f'}) \approx c_0 V_c^2 \frac{1}{\bar{q}^4} \frac{1}{\Delta} \tag{C.9}$$

where V_c is the dimensionless cube volume.